Experimental Thermal and Fluid Science 130 (2022) 110486

Contents lists available at ScienceDirect

Experimental Thermal and Fluid Science

journal homepage: www.elsevier.com/locate/etfs

Two-phase air-water flows in hydraulic jumps at low Froude number: Similarity, scale effects and the need for field observations

Jorge Estrella [a], Davide Wüthrich [a,b], Hubert Chanson [a,*]

[a] The University of Queensland, School of Civil Engineering, Brisbane, QLD 4072, Australia
[b] Delft University of Technology, Department of Hydraulic Engineering, 2600 Delft, the Netherlands

ARTICLE INFO

Keywords:
Hydraulic jump
Two-phase gas-liquid flow
Physical modelling
Similitude
Scale effects
Turbulence
Froude similarity
Reynolds number

ABSTRACT

A hydraulic jump is a region of rapidly-varied flow that is extremely turbulent. While the one-dimensional continuity and momentum principles have been successfully applied to express the relationships between upstream and downstream conditions, the three-dimensional equations cannot be resolved without some complicated turbulence closure, often involving two phases, i.e. air and water. Based upon a new dataset, the current investigation has the double objective of presenting a novel experimental investigation of the air-water flow characteristics in hydraulic jumps with a small Froude number ($Fr_1 = 2.1$) and discussing the potential scale effects involving several Reynolds numbers ($0.078 \times 10^5 < Re < 3.05 \times 10^5$). Four unique features are the low inflow Froude number $Fr_1 = 2.1$, the wide range of Reynolds numbers tested systematically, the broad amount of air-water flow properties investigated, and the relatively high Reynolds number ($Re = 3.05 \times 10^5$) achieved in the largest experiment. More than two dozen of parameters were tested systematically under Froude similar conditions. All the data demonstrated that the selection of relevant (air-water) flow property(ies) used to assess similarity and scale effects is most essential. Further the concept of similarity and scale effects must be linked to specific flow conditions. At low Froude number ($Fr_1 = 2.1$), the present results showed that many hydraulic jump properties could not be extrapolated from laboratory study to full scale hydraulic structures without substantial scale effects. These findings have profound implications for engineering design applications, often operating with Reynolds numbers in excess of 10^5.

1. Introduction

A hydraulic jump is a stationary turbulent discontinuity from an upstream supercritical flow to a downstream sub-critical motion [2,57]. The transition is sudden and most jumps involve a vigorously tumbling flow region, called roller, where much kinetic energy is being lost (Fig. 1). A hydraulic jump is a region of rapidly-varied flow that is extremely turbulent and is associated with the development of large-scale turbulence, surface waves and spray, energy dissipation and air entrainment [58,36]. While the one-dimensional equations of conservation of mass and momentum have been successfully applied to express the relationships between upstream and downstream flow conditions [41,40], the three-dimensional equations cannot be resolved without some complicated turbulence closure, often involving two phases, i.e. air and water (Fig. 1B).

The first successful air-water flow measurements in hydraulic jumps were reported by Rajaratnam [52] and Schröder [59]. Resch and Leutheusser [56] showed the differences between partially-developed and fully-developed inflow conditions on the air-water flow properties and turbulent mixing. In the last twenty-five years, significant progresses were achieved experimentally, mostly in laboratory (e.g. [45,22,47,64,67,43]), with the seminal field study of Valle and Pasternack [63], and more recently numerically [44]. These studies documented the vertical distributions of void fractions and interfacial velocities in hydraulic jumps, typically with relatively large inflow Froude numbers. The results showed that the void fraction distributions were functions of the inflow Froude number, with increasing rate of air entrainment with increasing Froude numbers. The velocity profiles commonly presented a lower high-velocity jet, a shear zone with a high-velocity gradient $\partial V/\partial y$, and a recirculation region above, as sketched in Fig. 1A [53,22].

Most research to date was conducted with relatively large inflow Froude numbers ($Fr_1 > 3$), leaving the air-water flow properties of hydraulic jumps at low inflow Froude numbers mostly under-studied, with

* Corresponding author.
E-mail address: h.chanson@uq.edu.au (H. Chanson).

https://doi.org/10.1016/j.expthermflusci.2021.110486
Received 21 May 2021; Received in revised form 21 June 2021; Accepted 16 July 2021
Available online 24 July 2021

a few exceptions [47,72]. The present study is based upon a completely new experimental investigation developed with two key objectives: (a) to examine accurately the two-phase flow properties in a breaking jump with a small Froude number: $Fr_1 = 2.1$, and (b) to discuss potential scales effects in terms of several air-water flow parameters for Reynolds numbers across nearly two orders of magnitude, i.e. $7.7 \times 10^3 < Re < 3.1 \times 10^5$. In absence of prototype data, a set of related queries is: what minimal model size, e.g. in terms of Reynolds number values, is required in the physical model to observe scale-independent air-water flow properties? Is there an asymptotic behaviour, or do these parameters continue to increase with increased model size and Reynolds number? The current work intends to provide answer to these issues, expanding the earlier studies performed with larger Froude numbers ($3.8 < Fr_1 < 8.5$), typically covering a smaller range of Reynolds numbers, with a new broader data set undertaken with $Fr_1 = 2.1$, and will show the needs for field observations.

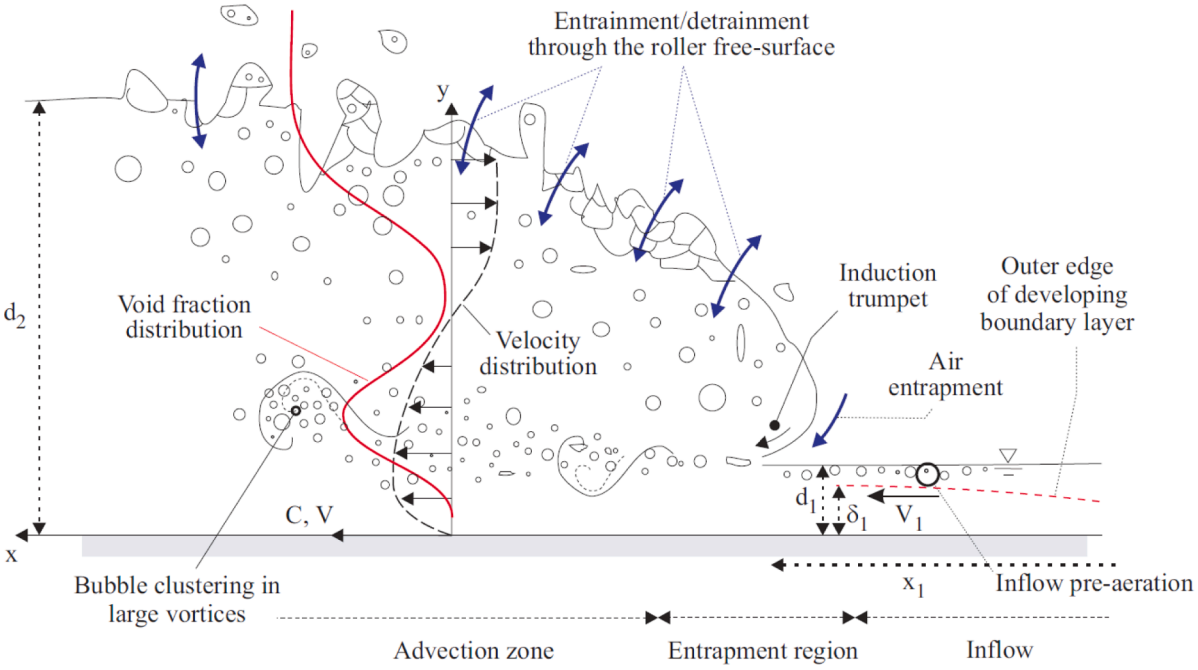

(A) Definition sketch of a hydraulic jump with a breaking roller in a smooth horizontal rectangular channel

(B) Hydraulic jump for $Fr_1 = 2.1$, $Re = 1.97 \times 10^5$ m, $d_1 = 0.097$ m, $x_1 = 1.5$ m, B = 0.5 m, shutter speed: 1/500 s - Flow direction from right to left, with the dual-tip phase-detection probe facing downstream

Fig. 1. Hydraulic jump at low Froude number.

2. Similarity, physical models and methodology

2.1. Presentation

A physical modelling investigation is expected to deliver a reliable prediction of the performances of a prototype flow motion [49,12]. The modelling approach must rely upon the fundamental principles of similitude [55]. Dimensional analysis is the basic procedure to generate the relevant dimensionless variables [3,40]. The outputs of any physical experiment may be described quantitatively by some mathematical function, with at least one dependent variable, while the remaining variables are independent variables [33]. Considering the case of a steady turbulent hydraulic jump flow in a rectangular channel (Fig. 1A), a dimensional analysis yields a series of dimensionless relationships in terms of the two-phase air-water flow properties at a location (x,y,z) in the breaking roller, as function of the fluid and physical properties, the channel geometry, and the inflow conditions.:

$$C, \frac{V_x}{V_c}, \frac{v_x^2}{V_c^2}, \frac{P}{\rho \times g \times d_c}, \frac{L_t}{d_c}, T_t \times \sqrt{\frac{g}{d_c}}, \frac{D_{ab}}{d_c}, \frac{N_c \times d_c}{V_c}, \ldots = F \left(\begin{array}{c} \frac{x}{d_c}, \frac{y}{d_c}, \frac{z}{d_c}, \\ \frac{B}{d_c}, \frac{k_s}{d_c}, \theta, \frac{x_1}{d_c}, \\ \frac{\delta_1}{d_c}, \frac{V_1}{V_c}, \frac{v_1'}{V_c}, \\ \rho \times \frac{V_c \times d_c}{\mu}, \frac{\rho \times V_c^2 \times d_c}{\sigma}, \ldots \end{array} \right) \quad (1)$$

where C is the local void fraction, V_x the interfacial longitudinal velocity, v_x a turbulent velocity fluctuation, P the local pressure, L_t a local turbulent length scale, T_t a turbulent time scale, D_{ab} a characteristic bubble size, N_c the number of bubble clusters per second, x, y and z are respectively the longitudinal, transverse and vertical coordinates, ρ and μ the water density and dynamic viscosity respectively, σ the surface tension between air and water, g is the gravity acceleration, B the channel width, k_s the equivalent sand roughness height of the channel boundary, θ the angle between the invert and the horizontal, x_1 the longitudinal coordinate of the roller toe, d_1 the inflow depth, δ_1 the inflow boundary layer thickness, V_1 the inflow velocity, v_1' a characteristic turbulent velocity at the inflow (Fig. A).

Eq. (1) expresses the dimensionless two-phase turbulent flow properties at a position (x,y,z) within the roller as functions of the non-dimensional inflow properties, fluid properties and channel geometry using the critical flow depth and velocity, i.e. d_c and V_c, as the characteristic length and velocity scales respectively. For a rectangular channel, the critical flow depth is related to the water discharge: $d_c = (Q^2/(g \times B^2))^{1/3}$, with Q the water discharge, and the critical flow velocity is: $V_c = (g \times d_c)^{1/2} = (g \times Q/B)^{1/3}$. In the right hand side of Eq. (1), the 9th, 11th and 12th terms are some Froude number Fr, Reynolds number Re and Weber number We. The Vaschy-Buckingham theorem implies further that any non-dimensional parameter number could be replaced by a combination of other non-dimensional parameters and itself. Simply, the Froude, Reynolds or Weber number may be replaced by the Morton number Mo defined as:

$$Mo = \frac{We^3}{Re^4 \times Fr^2} = g \times \frac{\mu^4}{\rho \times \sigma^3} \quad (2)$$

When the same fluids, i.e air and water herein, are used in laboratory and prototype, the Morton number is an invariant and the situation introduces a further constraint upon the dimensional analysis [51]. Thus, for a hydraulic jump study, Eq. (1) is best expressed as:

$$C, \frac{V_x}{V_c}, \frac{v_x^2}{V_c^2}, \frac{P}{\rho \times g \times d_c}, \frac{L_t}{d_c}, T_t \times \sqrt{\frac{g}{d_c}}, \frac{D_{ab}}{d_c}, \frac{N_c \times d_c}{V_c}, \ldots = F_3 \left(\begin{array}{c} \frac{x}{d_c}, \frac{y}{d_c}, \frac{z}{d_c}, \\ \frac{B}{d_c}, \frac{k_s}{d_c}, \theta, \frac{x_1}{d_c}, \\ \frac{\delta_1}{d_c}, \frac{V_1}{\sqrt{g \times d_1}}, \frac{v_1'}{V_1} \\ \rho \times \frac{V_1 \times d_1}{\mu}, \frac{g \times \mu^4}{\rho \times \sigma^3}, \ldots \end{array} \right) \quad (3)$$

Implicitly, this approach assumes that the viscous effects are of higher significance compared to the surface tension in full-scale prototype conditions [70,24]. In Eq. (3), the Froude and Reynolds numbers, Fr_1 and Re respectively, are defined more conventionally using the inflow depth d_1 and the inflow velocity V_1 as characteristic length and velocity scales:

$$Fr_1 = \frac{V_1}{\sqrt{g \times d_1}} \quad (4)$$

$$Re = \rho \times \frac{V_1 \times d_1}{\mu} \quad (5)$$

In a hydraulic jump, the momentum considerations demonstrate the significance of the inflow Froude number [1,57] and the selection of the Froude similitude derives implicitly from fundamental theory [35,19]. Between a laboratory model and a field application, the Froude and Reynolds number cannot be kept constant, when the same fluids are used. In practice, a Froude and Morton similitude is undertaken and the experiments must be conducted in a near-full-scale facility operating at relatively large Reynolds numbers to minimise viscous scale effects.

Herein, new experiments were repeated with an identical Froude and Morton number at different geometric scales, to test specifically the scale effects in terms of the Reynolds number impacting the multiphase gas–liquid flow properties in a hydraulic jump with a marked roller and $Fr_1 - 2.1$, within nearly two orders of magnitude: $0.078 \times 10^5 < Re < 3.05 \times 10^5$. The largest experimental configuration corresponded to a Reynolds number comparable to, or larger than, that of the prototype hydraulic jumps commonly seen in man-made storm waterways and water treatment plants.

2.2. Physical models and instrumentation

The present investigation was conducted in three horizontal rectangular flumes at the Hydraulics Laboratory of the University of Queensland (Australia). Fig. 1B presents a photograph of an experimental flume in operation. The flumes were identical: the channel width was B = 0.50 m, the test section length was 3.2 m, the sidewalls were 0.40 m high and made of glass, the channel bed was horizontal (θ = 0) and made of HDPE. The inflow conditions to the test section were controlled by a vertical gate with a semi-circular shape (⌀ = 0.3 m). The upstream gate opening h was fixed during each experiment, and openings between h = 0.012 m and 0.130 m were used. The tailwater conditions were controlled by a vertical overshoot gate located at the downstream end of the test section.

In each flume, the water discharge was measured with a Venturi meter located in the supply line, designed according to British standards. The discharge measurement was accurate within ± 2%, and checked against independent observations of water depths upstream and downstream of the upstream gate. The clear-water flow depths were measured using rail-mounted point gages within ± 0.5 mm accuracy. The two-phase air-water flow properties were measured with some dual-tip

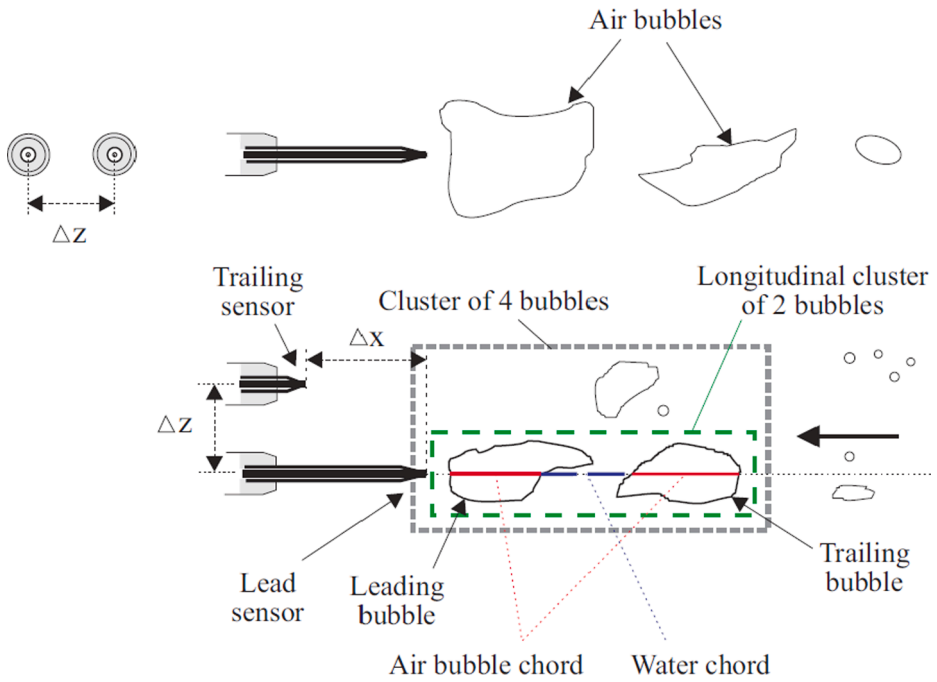

Fig. 2. Definition sketch of bubble cluster detection by a dual-tip phase-detection probe in air-water flow. Top: front view (left) sideview (right); Bottom: view in elevation.

phase detection conductivity probe (Fig. 2). Each dual-tip probe was equipped with two identical needle sensors with an inner diameter of 0.25 mm. The longitudinal distance between probe tips was $\Delta x_{tip} = 7.0$ mm, while the transverse distance between probe tips was $\Delta z = 2.2$. mm. The probes were manufactured at the University of Queensland and were excited by an electronic system (Ref. UQ82.518) designed with a response time of<10 μs. During the experiments, each probe sensor was sampled at 20 kHz for 45 s. The movement and location of the probe in the vertical direction were controlled by a fine adjustment system connected to a HAFCO™ digimatic scale unit with a vertical accuracy of<0.1 mm.

2.3. Signal processing

The processing of the phase-detection probe voltage output was based upon a single threshold technique, with the threshold being set at 50% of the air-water voltage range [62]. A number of air-water flow properties may be derived from the probe signal analysis [13]. These encompassed the void fraction C defined as the volume of air per unit volume, the bubble count rate F which is the number of bubbles impacting the probe tip per second, and the air chord time distribution where the chord time is defined as the time spent by the bubble on the probe tip. The air-water interfacial velocity V may be calculated as:

$$V = \frac{\Delta x_{tip}}{T} \quad (6)$$

where T is the average air-water interfacial time between the two probe sensors, deduced from a cross-correlation analysis [28]. The turbulence level Tu, characterising the fluctuations of the interfacial velocity between probe sensors, was estimated from the shapes of the cross-correlation R_{xy} and auto-correlation R_{xx} functions [26]. The analysis of signal auto-correlation function provided further information on the longitudinal bubbly flow structures [23]. The auto-correlation integral time scale T_{xx} represented a characteristic integral time scale of the large eddies advecting the air-water interfaces in the longitudinal direction. Herein, all the correlation calculations were undertaken on the raw probe signal output. Indeed, an analysis based upon thresholded signals would ignore the contributions of the smallest air-water particles [23]. In the present study, the smallest detectable bubbles were about the sensor size (i.e. 0.25 mm). All original files of 900,000 samples (sampling frequency of 20 kHz for 45 s) were segmented into 15 non-overlapping sub-segments of 60,000 samples each. At a given position, the results in terms of turbulence intensities and integral time scales were averaged values over the 15 non-overlapping sub-segments.

The identification of bubble cluster was undertaken based upon the analysis of the water chord between two successive air bubbles by the probe leading tip (Fig. 2). Based upon a near wake concept, the water chord time between two adjacent air particles was compared to the air chord of the leading bubble, recorded in the point of measurement:

$$t_{ch-w} < \phi \times t_{ch-a} \quad (7)$$

where $t_{ch\text{-}w}$ is the water chord time and $t_{ch\text{-}a}$ is the chord time of the leading bubble. The coefficient ϕ was taken as unity following previous studies [21,34]. The near wake clustering method is considered to be robust and effective because it relies on a comparison between the local characteristic air-water flow time scales. It is important to stress that the present data analysis was focused on the longitudinal air-water structure and did not consider any bubble travelling side-by-side [61,68]. Fig. 2 illustrates an example of four-bubbles cluster, of which only two are detected as part of a cluster.

Discussion

The influence of the dual-tip probe direction on air-water flow properties was carefully checked under controlled flow conditions for 0° and 180° [31]. A series of experiments were conducted by reversing the probe direction, i.e. repeating identical experiments with the probe sensors facing upstream and downstream. In terms of void fraction, the results were very close in the upper air-water flow region. In the lower air-water shear region, the experimental data with the probe sensor facing towards the roller toe tended to underestimate the local maximum in void fraction. The data showed no major difference in terms of the interfacial longitudinal velocity distributions. However, there were a significant difference on the bubble count rate F, because the probe facing downstream received lesser impact of the aerated flow. In summary, the present data, combined with the earlier study of Wang and Chanson [67], suggested that the probe orientation had a marked

effect on the bubble count rate data, some impact on the void fraction data in the (lower) air-water shear region, and no effect on the interfacial velocity distributions. In the following paper, the results are presented based upon data obtained with the probe sensors facing upstream.

Note that the dual-tip phase-detection probe recorded the velocity component along the direction of the probe sensor alignment, herein 0° and 180° with reference to longitudinal flow direction, although the hydraulic jump roller motion was three-dimensional and the instantaneous velocity direction could differ from the longitudinal direction. In hydraulic jumps with higher Froude numbers ($3.8 < Fr_1 < 8.5$), Wang and Chanson [65,64,67] analysed the probe signals manually, based upon the detection of individual bubbles, yielding instantaneous interfacial velocity data, with transverse velocity amplitudes $|V_z|$ up to 1–1.5 m/s, and ratios v_z'/v_x' of transverse to longitudinal velocity fluctuations between 0.5 and 1 typically [67]. The findings implied that the instantaneous "longitudinal" velocity component measurements (Eq. (6)) underestimated the instantaneous velocity magnitude.

2.4. Experimental flow conditions

The experiments were performed in three identical smooth horizontal channels, for a wide range of water discharges (Table 1). Measurements were conducted in a hydraulic jump with an inflow Froude number $Fr_1 = 2.1$, with inflow depths within $0.012\ m < d_1 < 0.130\ m$, for flow rates within $0.0039\ m^3/s < Q < 0.1535\ m^3/s$, and Reynolds numbers between 0.775×10^4 and 3.05×10^5. In Table 1, the present experimental flow conditions are compared to previous detailed air-water flow measurement experiments in hydraulic jumps on smooth horizontal channel, undertaken at different geometric scales, based upon an un-distorted Froude similitude. Note that previous works were conducted with larger inflow Froude numbers $3.8 < Fr_1 < 8.5$ and covered a smaller range of Reynolds numbers.

For most current experiments, the jump toe was located at a longitudinal position $x_1/d_c \approx 10$ (i.e. $x_1/d_1 \approx 15$), although the jump toe location was $x_1/d_c \approx 6$ (i.e. $x_1/d_1 \approx 9$) for the largest upstream gate opening $h = 0.130$ m. Previous velocity measurements in the same flume showed that the inflow was characterised by a partially-developed boundary layer for these conditions.

Since the inflow was smooth and horizontal, Eq. (3) may be simplified: i.e., $\theta = 0$ and $k_s \approx 0$. Further the present experiments were performed with constant Froude and Morton numbers, i.e. $Fr_1 = 2.1$ & $Mo = 2.5 \times 10^{-11}$. Thus Eq. (3) may be drastically reduced into:

$$C, \frac{V_x}{V_c}, \frac{v_x^2}{V_c^2}, \frac{P}{\rho \times g \times d_c}, \frac{L_t}{d_c}, T_t \times \sqrt{\frac{g}{d_c}}, \frac{D_{ab}}{d_c}, \frac{N_c \times d_c}{V_c}, \ldots = F_4 \left(\frac{x}{d_c}, \frac{y}{d_c}, \frac{z}{d_c}, \frac{B}{d_c}, \frac{x_1}{d_c}, \frac{\delta_1}{d_c}, \frac{v_1'}{V_1}, \rho \times \frac{V_1 \times d_1}{\mu} \ldots \right) \quad \text{for } Fr_1 = 2.1 \qquad (8)$$

Table 1
Detailed air-water flow measurement experiments in hydraulic jumps at different geometric scales, based upon un-distorted Froude similitude.

Reference	B (m)	h (m)	Q (m^3/s)	d_c (m)	x_1 (m)	d_1 (m)	x_1/d_c	Fr_1	Re	Instrumentation
Present study	0.50	0.012	0.0039	0.0184	0.19	0.012	10.3	1.9	7.75×10^3	Dual-tip phase-detection probes
		0.024	0.0146	0.0443	0.38	0.027	8.6	2.1	2.9×10^4	(Ø = 0.25 mm)
		0.045	0.0316	0.0741	0.71	0.045	9.6	2.1	6.3×10^4	
		0.070	0.0620	0.1162	1.11	0.071	9.6	2.1	1.2×10^5	
		0.095	0.0991	0.159	1.50	0.097	9.5	2.1	2.0×10^5	
		0.130	0.1535	0.213	1.20	0.130	5.6	2.1	3.05×10^5	
CHANSON and GUATIERI (2008)	0.25	--	0.0067	0.0418	0.50	0.0120	12.0	6.5	2.7×10^4	Single-tip phase-detection probes
	0.50	--	0.0360	0.0809	1.00	0.0232	12.4	6.5	7.2×10^4	(Ø = 0.35 mm)
	0.25	--	0.0062	0.0396	0.50	0.0132	12.6	5.1	2.5×10^4	
	0.50	--	0.0344	0.0785	1.00	0.0265	12.7	5.1	6.9×10^4	
	0.25	--	0.0096	0.0532	0.50	0.0129	9.4	8.4	3.8×10^4	
	0.50	--	0.0494	0.0999	1.00	0.02385	10.0	8.6	9.9×10^4	
MURZYN and	0.50	--	0.0310	0.0737	0.75	0.018	10.3	8.3	6.2×10^4	Dual-tip phase-detection probe
CHANSON (2008)	0.50	--	0.019	0.0528	0.75	0.018	14.2	5.1	3.8×10^4	(Ø = 0.25 mm)
CHANSON and CHACHEREAU (2013)	0.50	--	0.0627	0.117	1.5	0.0385	12.8	5.1	1.25×10^5	Dual-tip phase-detection probe (Ø = 0.25 mm)
WANG and CHANSON (2016)	0.50	0.012	0.0172	0.0494	0.50	0.013	10.1	7.5	3.4×10^4	Dual-tip phase-detection probe
		0.020	0.033	0.0763	0.83	0.020	10.9	7.5	6.6×10^4	(Ø = 0.25 mm)
		0.020	0.0347	0.0789	0.83	0.021	10.5	7.5	6.8×10^4	
		0.025	0.053	0.1047	1.04	0.027	9.9	7.5	1.1×10^5	
		0.030	0.0706	0.1267	1.25	0.033	9.9	7.5	1.4×10^5	
		0.030	0.0705	0.1266	1.25	0.033	9.9	7.5	1.4×10^5	
		0.020	0.0244	0.0624	0.83	0.021	13.3	5.1	4.7×10^4	
		0.020	0.0239	0.0615	0.83	0.021	13.5	5.1	4.8×10^4	
		0.030	0.046	0.0952	1.25	0.032	13.1	5.1	9.1×10^4	
		0.030	0.0463	0.0956	1.25	0.032	13.1	5.1	9.2×10^4	
		0.040	0.0701	0.1261	1.25	0.043	9.9	5.1	1.5×10^5	
		0.020	0.0179	0.0508	0.83	0.021	16.4	3.8	3.5×10^4	
		0.030	0.0342	0.0782	1.25	0.032	16.0	3.8	6.8×10^4	
		0.054	0.0812	0.1391	1.25	0.057	9.0	3.8	1.6×10^5	

Notes: B: rectangular channel width; d_c: critical flow depth; d_1: upstream water depth; Fr_1: upstream Froude number defined in terms of upstream flow depth; h: upstream gate opening; Q: discharge; Re: Reynolds number defined in terms of upstream flow depth; $S_o = 0$ (horizontal channels); x_1: longitudinal distance from upstream gate; (–): information not available. For all experiments, phase-detection probe signal outputs sampled at 20 kHz per sensor for 45 s.

3. Basic flow observations

The observations showed some hydraulic jump with a marked roller region for all investigated flow conditions. The jump features differed between Reynolds numbers, with the visual appearance of the roller becoming more turbulent with increasing Reynolds number while the inflow Froude number remained constant: $Fr_1 = 2.1$. Typical sideview photographs are presented in Fig. 3. For the smallest experiment, i.e. $Re = 7.75 \times 10^3$, no bubble entrainment was observed. For $Re = 2.9 \times 10^4$, very slight bubble entrainment was seen and no air bubble was detectable by the phase-detection probe sensors. For $Re > 2.9 \times 10^4$, the roller surface deformations became significant, indicating that neither gravity nor surface tension could prevent surface breakup. The entrained air in the "white water" region included a mix of bubbles, drops, foams, packets, with very energetic transient interfacial processes, e.g. breakup, coalescence, rebounds, collapses. Characteristic air-water surface features were evidenced at the roller free-surface. In the upper part of the roller, the instantaneous surface separating the water and atmosphere presented a complicated structure, with two interpenetrating and interacting phases (Fig. 1A). For relatively small void/liquid fractions (i.e. $C < 0.3$ or $(1\text{-}C) < 0.3$), one phase was connected and the other phase was dispersed, with C a volume-averaged void fraction. But the distinction, i.e. between connected and dispersed phases, became unclear in the intermediate region, i.e. $0.3 < C < 0.7$, where the two-phases are inter-connected [6,27]. Physically there were no rigid boundaries between the dispersed phase and intermediate regions. The intermediate region contained a mix of air and water entities constantly re-arranging as the result of collisions, deformations, coalescence and formation of "bubbles" and "droplets". To date, this region was rarely investigated experimentally, numerically or theoretically (Brocchini 2002 [5], [32]. For design engineers, a mean upper interface between white waters and atmosphere is often defined in terms of the characteristic elevation Y_{90} where the void fraction equals 0.90. This selection derives from both theoretical and experimental considerations [7], Wood 1985 [69], Chanson 1993 [10]), with the characteristic air-water elevation Y_{90} corresponding to the upper surface of the air-water flow region where the void fraction equals $C = 0.90$.

Physically, the breaking roller presented a number of key features which included the roller free-surface deformation, the presence and amount of air bubble entrainment, and a number of recurrent air-water surface features. Visual evidences highlighted the rapid deformation of the roller surface. Herein the deformation of the roller free-surface was mostly documented through sidewall photographs (Fig. 3). Fig. 3A to 3E illustrate the changes in roller shape, including strong surface deformation and air bubble entrainment, with increasing Reynolds numbers. Fig. 3D and 3E show the breaking of the roller surface, with more intense air entrainment at the roller toe and through the upper surface of the roller, highlighted by 'white waters'. A further evidence of the effect of the Reynolds number was the length of the air-water region. No air entrainment was observed for $Re = 7.75 \times 10^3$ (i.e. $d_1 = 0.012$ m & $V_1 = 0.65$ m/s). The finding was consistent with early studies suggesting an inception velocity for air entrainment about 1 m/s [37,30]. In the current study, individual air entrainment was seen for $Re > 2.9 \times 10^4$.

Some evidence of very strong turbulence was the amount of air-water surface features (Fig. 4). Such two-phase gas–liquid surface structures were discussed by Brocchini and Peregrine [6], Chachereau and Chanson [9], and Lubin et al. [42], and catalogued by Wüthrich et al. [73]. Characteristic air-water features included fingers, water droplets, slugs, mushrooms, crowns, boils and foam (Fig. 4). Despite their pseudo-random behaviour and short-lived existence, these instantaneous air-water structures showed some coherence and re-occurring patterns. These surface structures were subjected to strong transient deformations, leading to enhanced roller surface roughness (Fig. 4).

4. Two-phase air-water flow measurements

Systematic air-water flow measurements were performed in hydraulic jumps with a constant inflow Froude number of 2.1 corresponding to Reynolds numbers between 6.3×10^4 and 3.05×10^5 (Table 1). In the roller region of the hydraulic jump with $Fr_1 = 2.1$, some distinct air-water flow patterns were observed (Fig. 5), with similar trends to those observed at higher Froude numbers. This analysis will cover: void fraction (Section4.1), bubble count data (Section 4.2), interfacial velocities (Section 4.3) and bubble flow structures (Section 4.4). Results are discussed in terms of Scale effects in Section 5.

4.1. Void fraction: Theoretical considerations and experimental observations

At the upstream end of the roller, in the near-vicinity of the roller toe $(x\text{-}x_1)/d_c < 1$ (i.e $(x\text{-}x_1)/L_r < 0.2$ with L_r the roller length), the void fraction data showed some vertical profiles with a convex shape for $d_1 < y < Y_{90}$, somehow similar to void fraction observations in dam break wave on dry bed [14,15] and in breaking bores [39,60]. Herein, the roller length L_r is defined as the distance from the roller toe over which the mean free-surface level increased monotically. Simply, the vertical distribution of void fraction was convex next to the roller's leading edge, as sketched in Fig. 5, with a very large roller-depth-averaged void fraction. In that leading edge region, i.e. $(x\text{-}x_1)/L_r < 0.2$, the void fraction profile followed an analytical solution of the advective diffusion equation for air [60]:

$$C = 0.9 \times \left(\frac{y - d_1}{Y_{90} - d_1}\right)^N \quad \text{for } d_1 < y < Y_{90} \tag{9}$$

where N is positive, typically less than unity, and related to the depth-averaged void fraction C_m in the roller:

$$C_m = \frac{1}{Y_{90} - d_1} \times \int_{y=d_1}^{Y_{90}} C \times dy = \frac{0.9}{N+1} \quad \textit{within } d_1 < y < Y_{90} \tag{10}$$

while the dimensionless diffusivity follows:

$$D' = \frac{1}{N} \times \sqrt{1 - C} \times \left(\frac{C}{0.9}\right)^{1/N} \quad \textit{for } d_1 < y < Y_{90} \tag{11}$$

Implicitly, Eq. (9) suggests that self-aeration is predominantly an interfacial process with uncontrolled exchanges of air through the roller surface in the near-vicinity of the roller toe and that the turbulent diffusion of air is predominantly a vertical exchange, i.e. the turbulent diffusion of air in the vertical direction counterbalances exactly the buoyancy effect.

The depth-averaged diffusivity (D'_{mean}) may be integrated from Eqs. (9) and (10), leading to a correlation in terms of the depth-averaged void fraction C_m in the roller (i.e. $d_1 < y < Y_{90}$):

$$(D')_{mean} = \frac{1}{Y_{90} - d_1} \times \int_{t=d_1}^{Y_{90}} D' \times dz = 0.592 \times 0.119^{C_m} \times C_m^{0.861} \quad \text{for } 0 < C_m < 0.82 \tag{12}$$

with a normalised correlation coefficient $R^2 = 0.99893$. For $0 < C_m < 0.8$, the depth-averaged diffusivity is in average: $\overline{(D')_{mean}} \approx 0.0711$.

Further downstream of the roller toe: $1 < (x\text{-}x_1)/d_c < 1.8$ (i.e. $0.2 < (x\text{-}x_1)/L_r < 0.4$), in the roller region of the hydraulic jump, two distinct air-water regions were observed: one on the upper part of the roller and another in the developing shear region. A marked air-water region was observed in the upper flow region, corresponding to the free surface region characterised by a monotonically increasing void fraction with increasing vertical elevation. Physically, this upper region was characterised by large void fraction, splashes, recirculation, and interactions with the atmospheric boundary layer. Another distinct

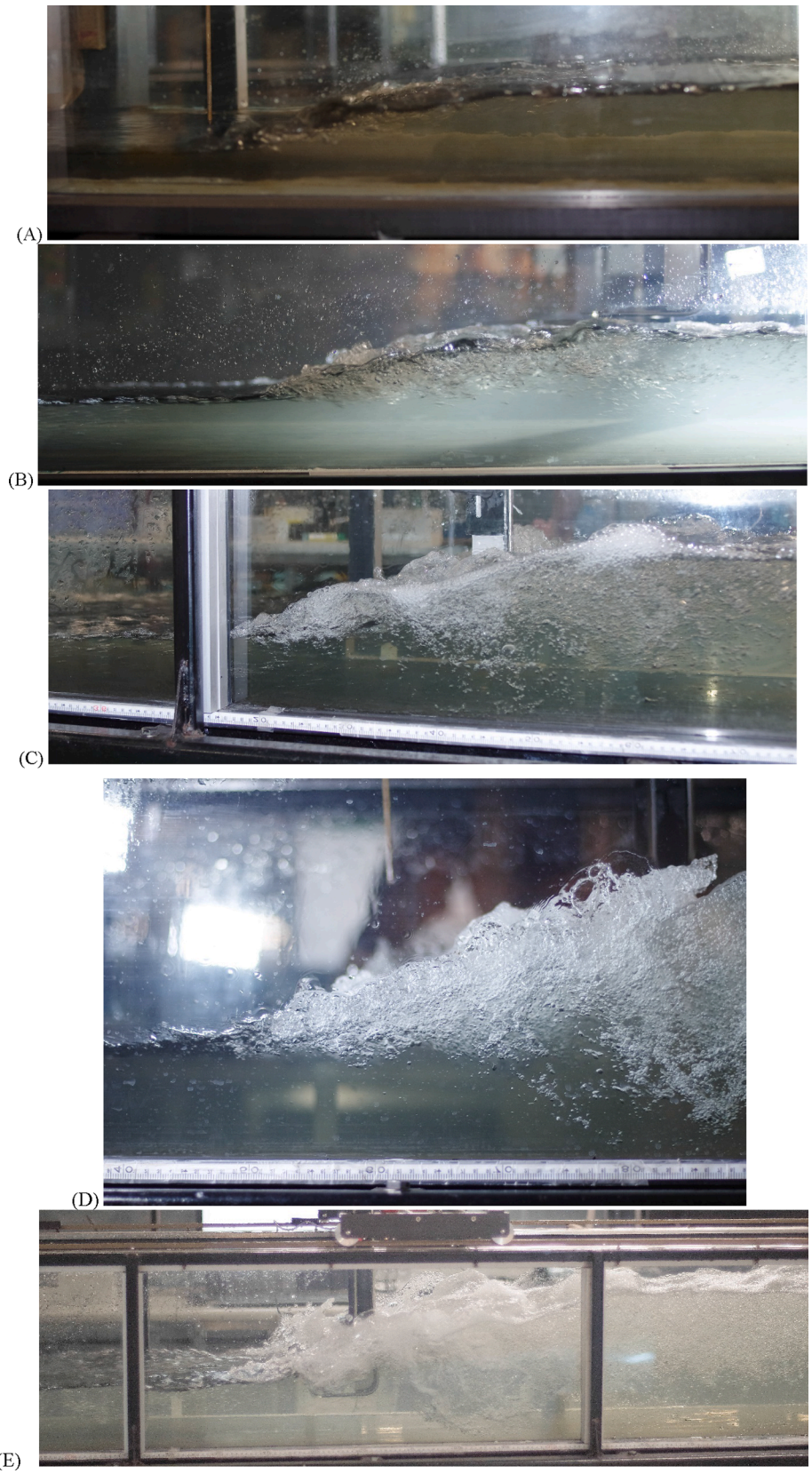

Fig. 3. Side views of hydraulic jumps at low Froude number $Fr_1 = 2.1$ with different Reynold numbers. (A) $Re = 2.9 \times 10^4$, $d_1 = 0.027$ m; (B) $Re = 6.3 \times 10^4$, $d_1 = 0.045$ m; (C) $Re = 1.2 \times 10^5$, $d_1 = 0.071$ m; (D) $Re = 2.0 \times 10^5$, $d_1 = 0.97$ m; (E) $Re = 3.05 \times 10^5$, $d_1 = 0.130$ m. Flow direction from left to right.

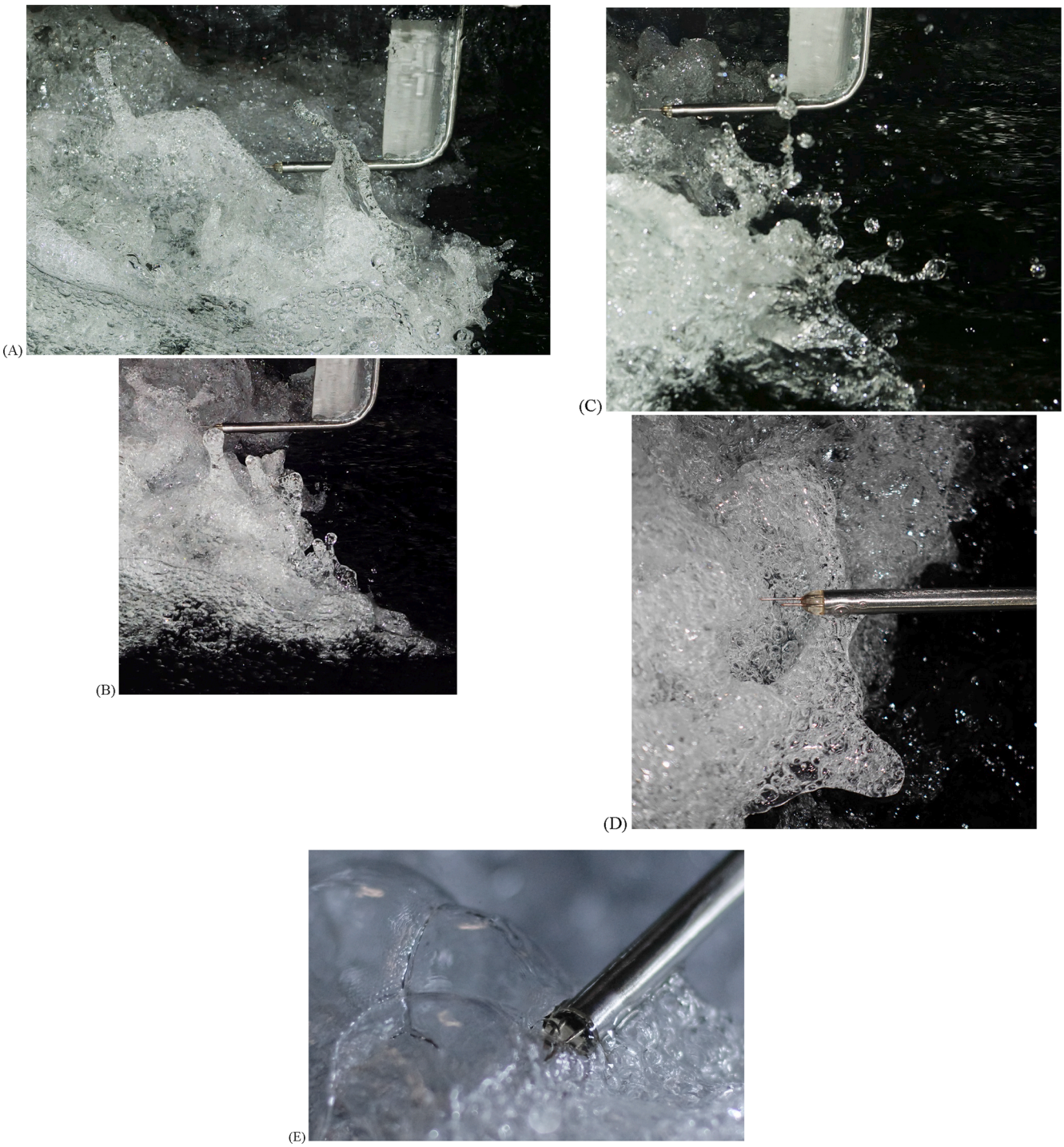

Fig. 4. Air-water surface features in hydraulic jump at low Froude number $Fr_1 = 2.1$ and $Re = 2.0 \times 10^5$ ($d_1 = 0.097$ m). Flow direction from right to left (unless stated) with dual-tip phase detection probe facing downstream. (A) Air-water projections and elongated air-water fingers above the roller free-surface (shutter speed: 1/500 s); (B) Thick air-water thumbs above the roller free-surface (shutter speed: 1/500 s); (C) Water droplets ejected above and upstream of the roller toe (shutter speed: 1/500 s); (D) Air-water features (hole, slug, mushroom) next to the impingement point (shutter speed: 1/2,000 s); (E) Foam structure (left) and air-water mix with flow direction from top right to bottom left (shutter speed: 1/2,000 s).

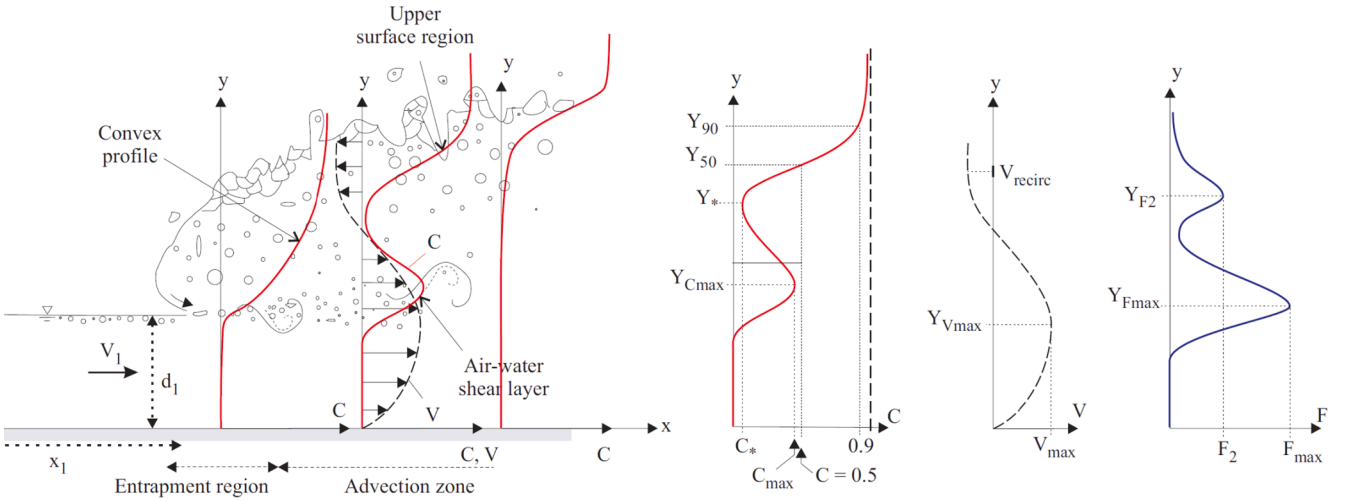

Fig. 5. Definition sketch of air-water flow properties in a hydraulic jump with a marked roller. Inset (Right): typical distributions of void fraction, interfacial velocity and bubble count rate in the advection zone.

air-water flow region was the lower region corresponding closely to the developing turbulent shear layer, with a local maximum in void fraction and a distribution following an advective diffusion trend. For the current experiments (Table 1), the lower air-water region was clearly observed at the largest Reynolds numbers, but tended to disappear at the lower Reynolds numbers. In the air-water shear layer, at the larger Reynolds numbers, the void fraction distributions were compared successfully with some analytical solution of the advective diffusion equation for air bubble [11,18]:

$$C = \frac{\frac{Q_{air}}{Q}}{\sqrt{4 \times \pi \times D^{\#} \times X'}} \times \left(exp\left(-\frac{\left(\frac{y}{d_1} - 1\right)^2}{4 \times D^{\#} \times X'} \right) + exp\left(-\frac{\left(\frac{y}{d_1} + 1\right)^2}{4 \times D^{\#} \times X'} \right) \right) \quad 0 < y < Y_* \tag{13}$$

where Q_{air} is the entrapped air flux, Q is the water discharge, $D^{\#}$ is a dimensionless air bubble diffusivity in the shear layer (typically derived from the best data fit), $X' = (x - x_1 + u_r/V_1 \times y)/d_1$, u_r the bubble rise velocity, Y* is the characteristic elevation corresponding a local minimum in void fraction above which the void fraction increased monotonically to unity (Fig. 4). Eq. (13) characterises the convective diffusion of air bubbles entrapped at the roller toe [29,18].

In the upper region, the void fraction distributions followed closely another solution of the advective diffusion equation for air bubbles [4,47]:

$$C = \frac{1}{2} \times \left(1 + erf\left(\frac{\left(\frac{y - Y_{50}}{d_1}\right)}{\sqrt{4 \times D^* \times \left(\frac{x - x_1}{d_1}\right)}} \right) \right) \quad Y_* < y < Y_{90} \tag{14}$$

where Y_{50} and Y_{90} are the characteristic elevations where C = 0.50 and 0.90 respectively, D* is a dimensionless air bubble diffusivity for the interfacial aeration through the roller free-surface and erf is the Gaussian error function:

$$erf(u) = \frac{2}{\sqrt{\pi}} \times \int_0^u exp(-t^2) \times dt \quad Y_* < y < Y_{90} \tag{15}$$

Eq. (14) was developed for interfacial aeration/de-aeration through the free-surface.

At the downstream end of the roller: $(x\text{-}x_1)/d_c > 1.8$ (i.e. $0.4 < (x\text{-}x_1)/L_r < 1$)), the air bubble motion in the roller was mostly driven by buoyancy. The void fraction distributions were compared successfully to a solution of the advective diffusion equation for interfacial aeration/de-aeration (Eq. (14)) for $Y_{10} < y < Y_{90}$. No air-water shear layer was distinguishable.

Eqs. (9), (13) and (14) are compared to experimental data in Fig. 6 for a selected flow condition ($Fr_1 = 2.1$ and $Re = 3.05 \times 10^5$). Typical void fraction distributions are presented in Fig. 6. Fig. 6 (Top) presents some data in the near-vicinity of the roller toe, i.e. at the upstream end of the roller, in which the flow aeration was predominantly an interfacial process with uncontrolled exchanges of air through the roller surface. Fig. 6 (Middle & Bottom) shows void fraction data in the first half of the roller, where the void fraction distribution was driven by a combination of convective diffusion of entrapped air in the air-water shear layer and interfacial aeration through the upper free-surface. In the second half of the roller, the de-aeration taking place at the free-surface is driven by buoyancy.

Overall, large amounts of entrained air were recorded in the breaking roller. In the air-water shear layer, the local maximum in void fraction C_{max} was observed to decrease with increasing distance from the roller toe $(x\text{-}x_1)$ (Fig. 7). Fig. 7 shows the longitudinal evolution of maximum void fraction C_{max} with the dimensionless co-ordinate. The data showed some effect of the Reynolds number, in particular for $Re < 1.2 \times 10^5$. That is, the maximum void fraction increased with the Reynolds number at a given cross-section $(x\text{-}x_1)/d_c$. The present data exhibited a longitudinal trend that was best correlated by:

$$C_{max} = exp\left(-\lambda \times \left(\frac{x - x_1}{d_c} \right)^{\gamma} \right) \quad Fr_1 = 2.1 \tag{16}$$

with the dimensionless coefficients λ and γ being functions of the Rey-

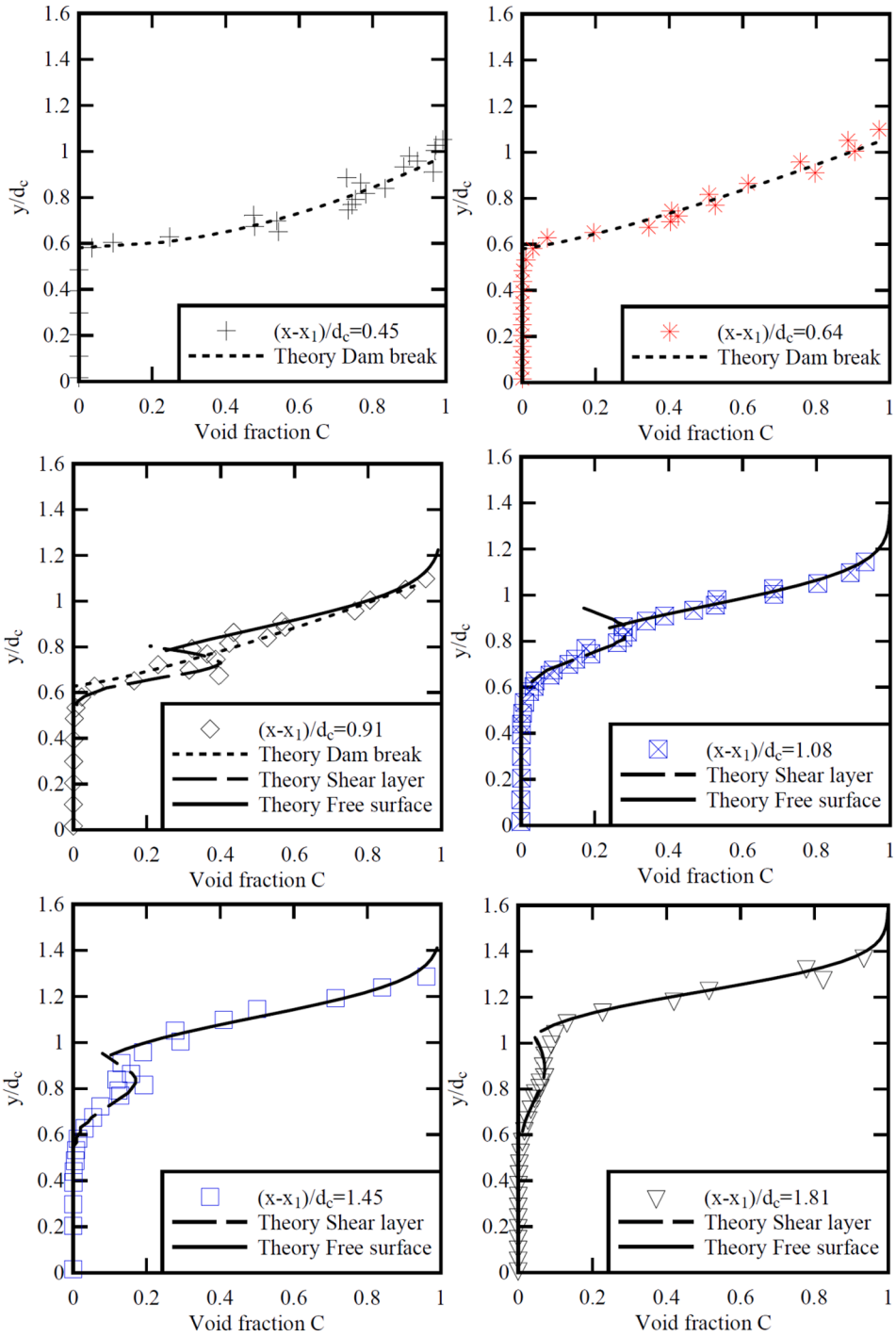

Fig. 6. Dimensionless distributions of void fraction in the hydraulic jump roller for $Fr_1 = 2.1$, $Re = 3.05 \times 10^5$, $d_1 = 0.130$ m. Comparison between experimental data and Eqs. (9) (Dam break), (13) (Shear layer) and (14) (Free-surface).

nolds numbe. For $1.2 \times 10^5 < Re < 3.0 \times 10^5$, the current data yielded $1.0 < \lambda < 1.5$ and $-0.9 < \gamma < 1.6$. Eq. (16) is shown in Fig. 7 for $Re = 3.0 \times 10^5$.

The dimensionless turbulent diffusivities $(D')_{mean}$ close to the roller front (Eq. (9)), $D^{\#}$ in the shear layer (Eq. (13)) and D^* in the upper free surface region (Eq. (14)) were deduced from the best data fit for all flow conditions. The results are presented in Fig. 8A as functions of the dimensionless distance to the jump toe $(x-x_1)/d_c$. While the data for both $(D')_{mean}$ (Eq. (9)) and $D^{\#}$ (Eq. (13)) showed little change along the roller length, the data for D^* showed a decreasing trend with increasing distance from the roller toe. This trend was likely to correspond physically to a marked change in the interfacial exchanges through the roller's free-surface. In the upstream section of the roller, the interfacial exchange was dominated by air entrainment into the roller [64], while further downstream, the interfacial exchange was associated with a de-aeration process.

In the air-water shear layer, the values of dimensionless diffusivity $D^{\#}$ ranged between 0.01 and 0.03 (Fig. 8B). In Fig. 8B, the current data are plotted against previous experimental studies [22,18,9]. Despite some scatter, the dimensionless diffusivity data were within the same order of magnitude, and almost independent of the longitudinal distance from the roller toe in the current study (Fig. 8B). The present trend

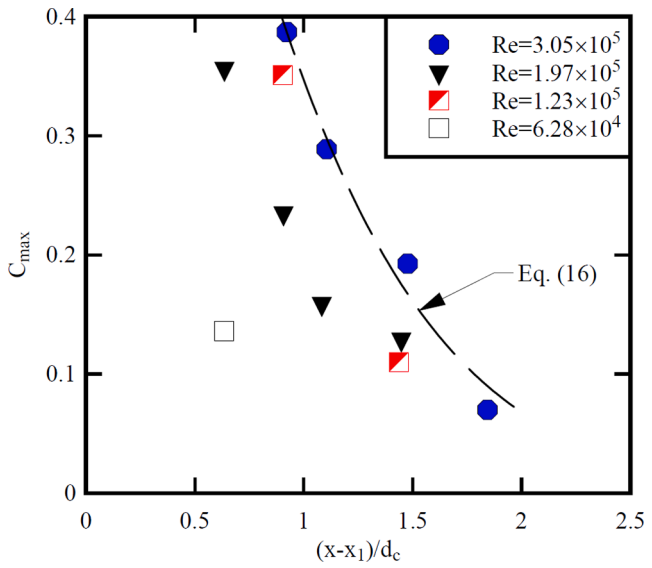

Fig. 7. Dimensionless longitudinal distributions of local maximum void fraction C_{max} in the air-water shear layer. Comparison with Eq. (16) with $\lambda = 1.06$ and $\gamma = 1.34$ for Re = 3.05×10^5.

however differed from experimental data obtained with large Froude numbers.

4.2. Bubble count data

Another key air-water parameter is the bubble count rate F. For a given void fraction, a high bubble count rate corresponds to a high fragmentation of the flow and large interfacial area. The bubble count rate data were recorded for a range of experimental flow conditions (Table 1). Fig. 9 presents typical vertical profiles of dimensionless bubble count rates $F \times d_c/V_c$. The data exhibited some vertical distributions that were comparable to earlier observations in breaking jumps [22,47,16]. The data highlighted a maximum bubble count rate F_{max} in the air-water shear layer, and a secondary peak F_2 in the upper free-surface region (Fig. 5). The peak in bubble count rate in the shear layer was linked to high levels of turbulent shear stresses breaking the entrained bubbles into finer particles, which were advected by the high velocities, yielding an important number of bubbles detected by the probe sensor.

Fig. 10 presents the characteristic bubble count rates F_{max} and F_2 as functions of the dimensionless distance to the roller toe for all Reynolds numbers, as well as their characteristic elevations, Y_{Fmax} and Y_{F2} respectively. The experimental data in terms of the maximum count rate F_{max} suggested an initial increase in F_{max} with increasing distance from the roller toe, followed by an pseudo-exponential decay with distance further downstream (Fig. 10, Top left). Such a trend was first reported in plunging jet flows [4], and also in hydraulic jumps with higher Froude numbers [75]. Importantly, the dimensionless maxima $F_{max} \times d_c/V_c$ and $F_2 \times d_c/V_c$ were seen also to increase with increasing Reynolds number at a given location for $Fr_1 = 2.1$.

For all flow conditions, the location of maximum bubble count rate F_{max} in the air-water shear layer was systematically below the elevation of the secondary peak F_2 in the upper free-surface (Fig. 10).

4.3. Interfacial velocity data

The air-water interfacial velocity data were deduced from a cross-correlation analysis of the dual-tip conductivity probe signals (Eq. (6)). An implicit limitation of the technique was the lack of reliable cross-correlation outputs in the regions where the sign of the interfacial velocity changed rapidly during the sampling duration, herein 45 s. Such a situation was typical of the transition between the air-water shear layer and upper free-surface regions, where large-scale vortices induced velocity shifts between positive and negative values. Fig. 11 presents typical dimensionless distributions of interfacial velocities V/V_c in the air-water region of the breaking roller, where V is the time-averaged interfacial velocity.

The experimental results highlighted some key features for all flow conditions. Along the roller region, the velocity profiles resembled that of a wall jet [53,50,22]. That is, a high-velocity jet next to the invert caused by the high-velocity impinging flow, an air-water shear zone with some high velocity gradient $\partial V/\partial y$, and an upper region above with lesser velocities. With increasing longitudinal co-ordinate, the velocity profiles deformed, towards a pseudo-uniform velocity distribution, asymptotically approaching the profile in an open channel far downstream [71]. This is illustrated in Fig. 11.

The velocity profiles are further compared for different Reynolds numbers in Fig. 11. Overall, the velocity data were qualitatively in agreement and quantitatively close for all Reynolds numbers. Some small difference was seen in the downstream part of the roller, where the velocity profiles tended to become more uniform for the lowest Reynolds numbers. That is, the transition from wall-jet to pseudo-uniform profiles shifted further downstream at the highest Reynolds number (Fig. 11, Bottom right). This could possibly be linked to the roller length, which was more affected by the Reynolds number.

For completeness, any time-averaged recirculation in the roller upper region was hardly detectable, in the present study, even with a reversed probe orientation. While, instantaneous reverse motion was visually observed, as well as recorded in normal speed and high-speed video movies [31], the time-averaged results did not show negative velocities. This differed from interfacial velocity distributions in hydraulic jumps at higher Froude numbers [9,67,43]. And this might imply relatively small velocity fluctuations, possibly associated with lesser turbulent dissipation in weak hydraulic jumps.

The turbulence intensity Tu, characterising the fluctuations in interfacial velocity, was estimated from the cross-correlation analysis between the two probe tip signals. The method was based on the relative width of the auto- and cross-correlation functions [38,26]. Some typical data are presented in Fig. 12A, as dimensionless distributions of turbulence intensity in the breaking roller. At a given location, the vertical profiles exhibited a characteristic trend with increasing vertical elevation. Namely Tu increased with elevation for $y/d_c > 0.4$ to 0.5. Below (i.e. $y/d_c < 0.4$), the flow aeration was limited and the data quality implicitly reduced. Along the roller length, the turbulence intensity tended to decrease with increasing distance from the roller toe.

Some additional processing of the dual-tip phase-detection probe signals yielded the time scales of turbulence of the air-water flow region [16,23]. The integral time scale T_{xx} represented some time scale estimate of largest coherent structures advecting the air-water structures, thus characterising the longitudinal flow structure. Fig. 12B shows typical vertical distributions of the auto-correlation integral time scale T_{xx} in the breaking roller. Next to the channel bed, the invert prevented the development of large-sized turbulent structures, and the smallest integral time scales were seen (Fig. 12B). At a fixed longitudinal distance from the roller toe, the integral time scales increased with increasing vertical elevation, for $y/d_c > 0.4$ to 0.5. Further T_{xx} tended to decrease with increasing longitudinal distance from the roller toe. Quantitatively, the turbulent time scales were smaller than 50 ms.

4.4. Bubbly flow structure

4.4.1. Bubble chord lengths

Visual observations showed a lot of entrained air bubbles for Re > 6.3×10^4 (Figs. 1B, 3 & 4). The bubble count rate data indicated a strong fragmentation of the roller's air-water flow, with maximum bubble count rate in excess of 50 bubbles per unit time. While visual observations, photographs and video movies showed a range of millimetric

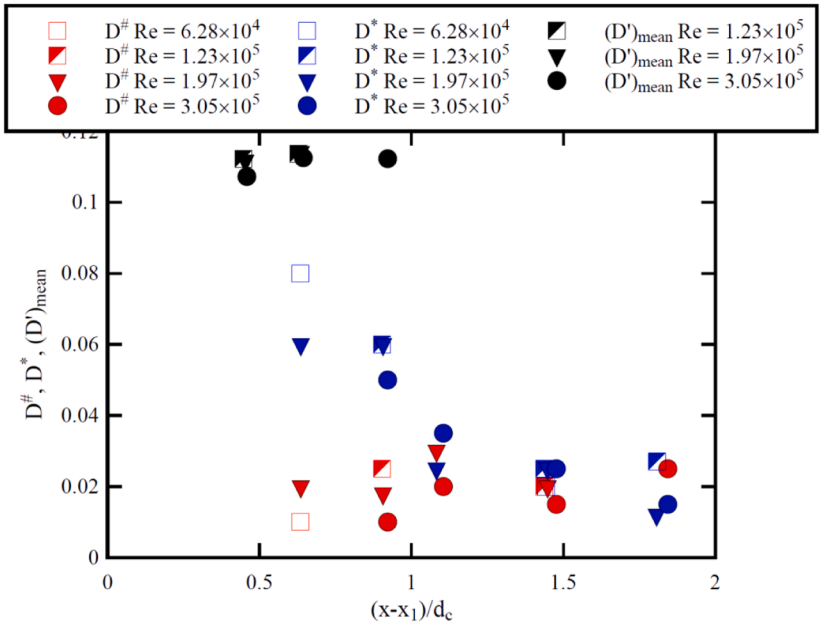

(A) Dimensionless air bubble turbulent diffusivities $(D')_{mean}$ (Eq. (4-1)), $D^{\#}$ (Eq. (4-5)), and D^{*} (Eq. (4-6))

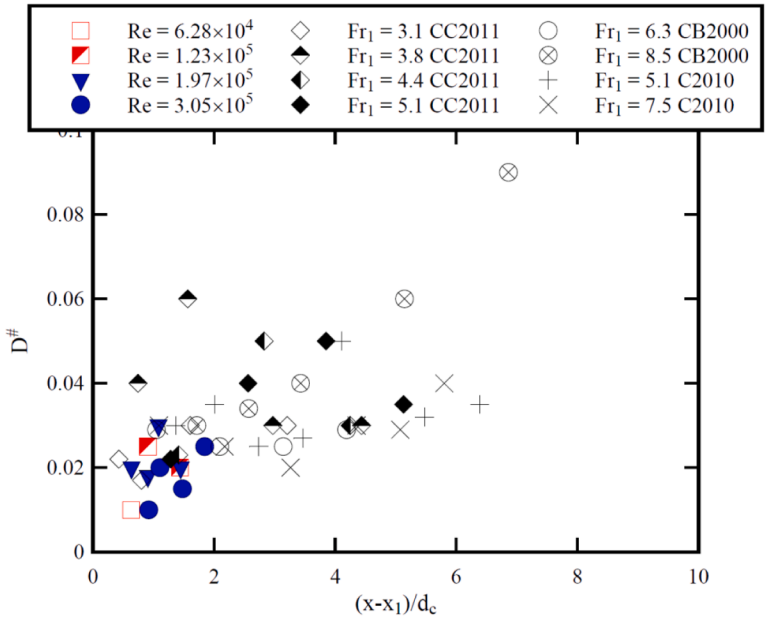

(B) Dimensionless air bubble turbulent diffusivity $D^{\#}$ in the air-water shear layer - Comparison with previous studies (Chanson and Brattberg 2000 [CB2000] , Chachereau and Chanson 2011 [CC2011], Chanson 2010 [C2010])

Fig. 8. Dimensionless air bubble turbulent diffusivities as a function of the dimensionless distance to the jump toe $(x\text{-}x_1)/d_c$.

bubbles, this section presents measurements of bubble chord lengths, calculated as $V \times t_{ch}$.

The probability distribution functions of bubble chord lengths were calculated in the air-water shear layer. Typical bubble chord length distributions are presented in Fig. 13, at the location where F was maximum, i.e. $y = Y_{Fmax}$. In Fig. 13, each data symbol represents the probability of bubble chord length in 1 mm chord time interval, e.g. the probability of bubble chord length between 1 mm and 1.5 mm is the symbol labelled 1 mm. Bubble chord times >20 mm are regrouped in the last symbol (20 mm). Overall, the experimental data showed a broad spectrum of chord lengths at all investigated locations for all flow conditions. The results were qualitatively comparable to earlier data sets obtained in hydraulic jumps with larger Froude numbers [16,9,43]. Altogether, the bubble chord length distributions were skewed with a preponderance of smaller bubble sizes relative to the mean (Fig. 13). Although the probability of air bubble chord lengths was the largest for chord sizes between 0 and 2 mm, it should be noted the amount of bubbles >20 mm in the air-water shear layer (Fig. 13, last data point). Such "large bubbles" were air entities, encompassing large enclosed air bubbles, non-enclosed "bubbles" as well as air gaps between water

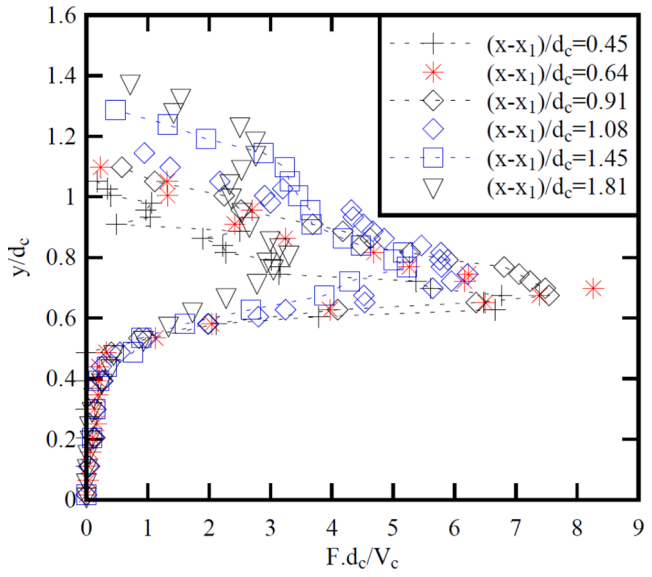

Fig. 9. Dimensionless distributions of bubble count rate in the hydraulic jump roller for $Fr_1 = 2.1$, $Re = 3.05 \times 10^5$, $d_1 = 0.130$ m.

features.

The probability distribution functions of bubble chord length tended to follow in average a shape close to log–normal distribution or a gamma distribution. At two cross-sections, i.e. $(x\text{-}x_1)/d_c = 0.63$ and 1.45, the bubble size distributions were compared for four Reynolds number (Fig. 13). Although all the bubble chord sizes were mostly millimetric for all Reynolds numbers, the data indicated skewer distributions towards smaller bubble chords for the largest Reynolds numbers, possibly linked to the larger turbulent stresses. Altogether, the results showed that the bubble sizes were not scaled based upon the geometric scaling ratio for a Froude similitude. The finding was consistent with some seminal literature on air-water flows [54,70,11].

4.4.2. *Bubble clustering*

Both the bubble count rate and bubble chord data showed a large number of entrained bubbles, with bubble sizes spanning over more than two orders of magnitude. The entrained air bubbles interacted with the turbulent structures, yielding some turbulent dissipation and the formation of bubble clusters [16]. Visual observations further highlighted some strong preferential bubble accumulation, i.e. clustering, in the air-water shear layer of the breaking roller. The study of preferential concentration of bubble is important in engineering applications to infer whether the formation frequency responds to some particular frequency of the flow [8,20]. The level and intensity of clustering may give a measure of the magnitude of bubble-turbulence interactions and associated turbulent dissipation.

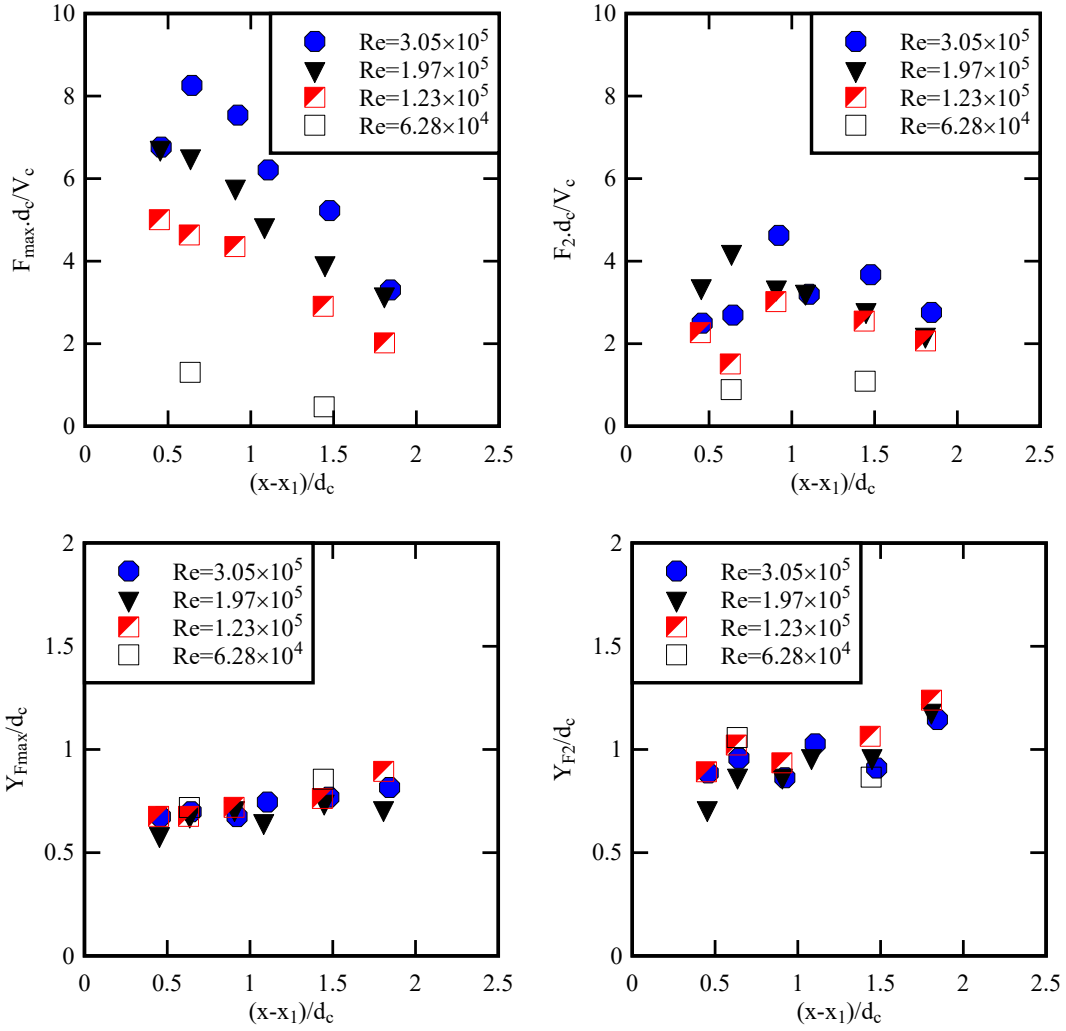

Fig. 10. Longitudinal distributions of maximum bubble count rate $F_{max} \times d_c/V_c$ and $F_2 \times d_c/V_c$, and their characteristic elevations Y_{Fmax}/d_c and Y_{F2}/d_c respectively.

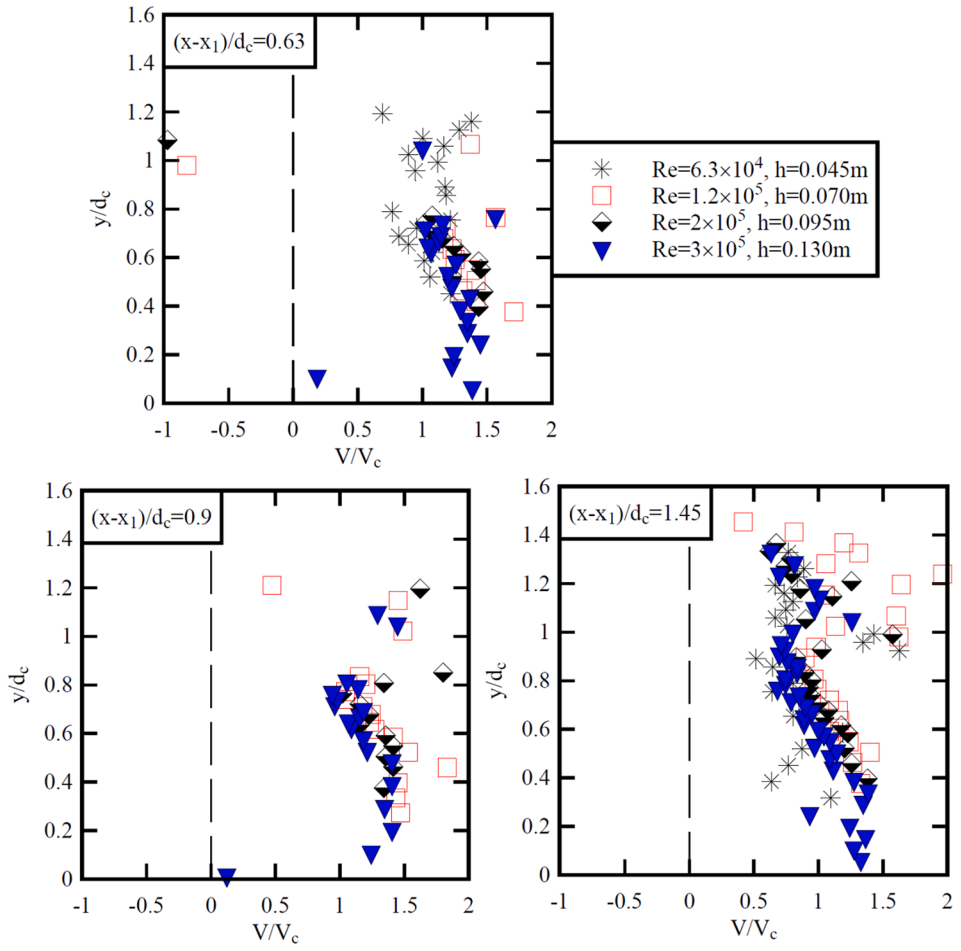

Fig. 11. Dimensionless distributions of interfacial velocities for $Fr_1 = 2.1$ at $(x\text{-}x_1)/d_c = 0.63$, 0.9 and 1.45. Same legend for all graphs.

In a hydraulic jump, the clustering characteristics may deliver some measure of the level of bubble-turbulence interactions, of the vorticity production rate, and of the associated energy dissipation. The experimental data showed large bubble cluster rates in the air-water shear layer. The dimensionless cluster rate $N_c \times d_c/V_c$ tended to decrease with increasing longitudinal distance from the roller toe (Fig. 14A). Figs. 14 and 15 present some typical properties of bubble clusters in the developing shear layer at the characteristic location $y = y_{Fmax}$ where the bubble count rate was maximum $F = F_{max}$. The average number of bubbles per cluster ranged from 2.2 to 3, although this value underestimated the total number of bubbles in a cluster, since it only considered longitudinal clustering (Fig. 2). The cluster size showed a decrease with increasing distance from the roller toe, for a given Reynolds number. A large proportion of bubbles were clustered, with a percentage of bubbles in cluster decreasing with increasing streamwise distance. The distributions were strongly skewed towards two bubbles per cluster. While the average number of bubbles per cluster was less than three, larger clusters in excess of 10 bubbles were observed, although rarely. Fig. 15 presents typical histograms of the number of bubbles per cluster. In average, the chord times of clustered bubbles were larger than the average bubble chord times for all investigated flow conditions. In a cluster, the ratio of the lead bubble chord to average cluster bubble chord was equal to 1.37 in average: that is, the lead particle chord was larger than the typical cluster bubble chord (Data not shown).

The intensity of bubble clustering may deliver some measure of bubble-turbulence interrelations and turbulent dissipation. The present data highlighted that the bubble clustering affected a large proportion of particles, especially at higher Reynolds numbers. The outcomes implied that the interactions between entrained bubbles and turbulent structures were not scaled adequately with the Froude similarity, in line with two earlier studies conducted at higher Froude numbers [24,66]. This is illustrated in Fig. 14B at a given cross-section, for two Froude numbers.

Finally, the present data were recorded for a Froude number of 2.1. A number of trends differed compared to earlier studies [16,18,66]. It is believed that a key difference was the lower Froude number, i.e. $Fr_1 = 2.1$, as well as the broader Reynolds number range investigated herein ($6.3 \times 10^4 < Re < 3.0 \times 10^5$).

5. Discussion: Similarity and scale effects

The Vaschy-Buckingham theorem implied that only a small number of independent dimensionless parameters are relevant to investigate the air entrainment in a hydraulic jump using the same fluids in laboratory and in full-scale prototype (Eq. (3)). Traditionally, the selection of the Froude similitude is based upon some basic theoretical considerations [57,35,40]. When both Froude and Morton similarities are selected, as in the current study, the Reynolds number differs between the various experiments, herein performed with an identical Froude number $Fr_1 = 2.1$. The current comparative analyses revealed that, for a hydraulic jump with $Fr_1 = 2.1$, a number of basic air-water flow characteristics could not be tested in small-size laboratory experiments, and many properties could not be extrapolated to large-size prototype structures without significant scale effects. This is illustrated in Figs. 16–19, presenting the dimensionless maximum bubble count rate in the air-water shear layer, turbulent time scales and some key bubble clustering characteristics as functions of the Reynolds number. As an illustration, Figs. 16 and 19 show that several parameters increased monotonically

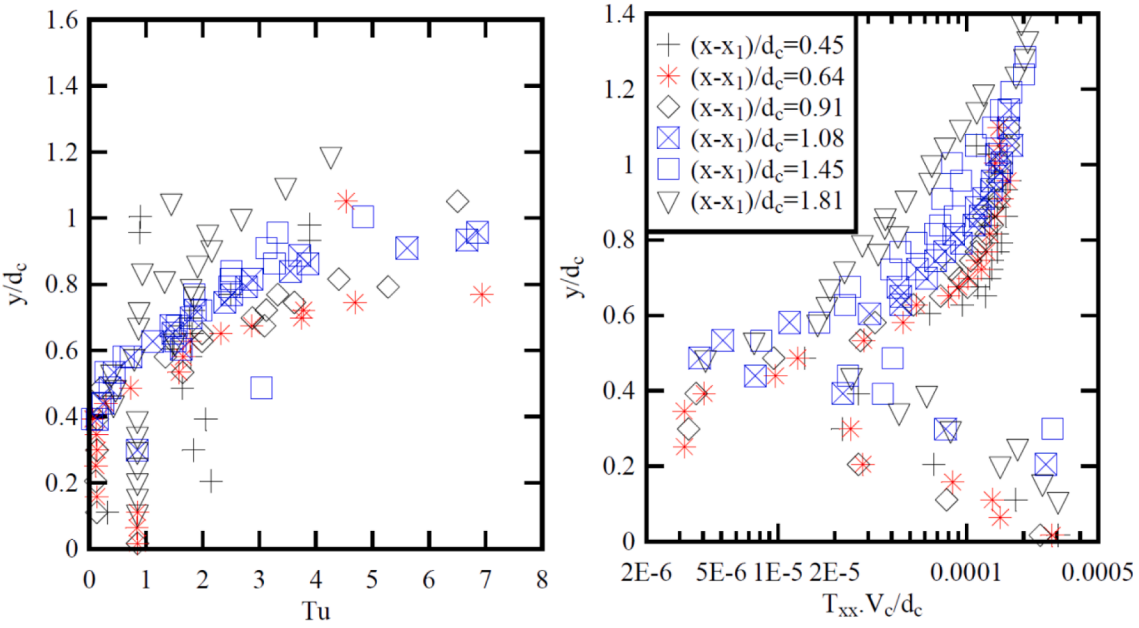

(A, Left) Turbulence intensity Tu

(B, Right) Auto-correlation turbulent time scale $T_{xx} \times V_c/d_c$

Fig. 12. Dimensionless distributions of turbulence intensity Tu and turbulent time scale $T_{xx} \times V_c/d_c$ for $Fr_1 = 2.1$, $Re = 3.05 \times 10^5$ ($d_1 = 0.130$ m). Same legend for both graphs.

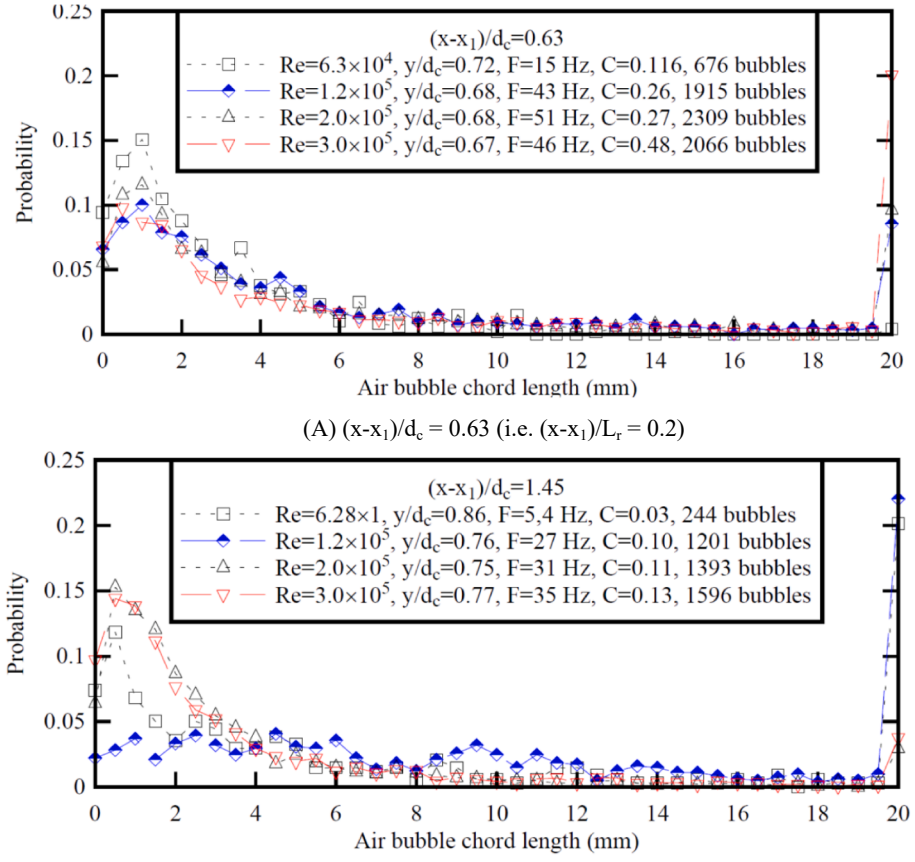

(A) $(x\text{-}x_1)/d_c = 0.63$ (i.e. $(x\text{-}x_1)/L_r = 0.2$)

(B) $(x\text{-}x_1)/d_c = 1.45$ (i.e. $(x\text{-}x_1)/L_r = 0.4$)

Fig. 13. Comparison of bubble chord length distributions at elevation Y_{Fmax} of maximum bubble count rate ($F = F_{max}$) in the air-water shear layer for $Fr_1 = 2.1$.

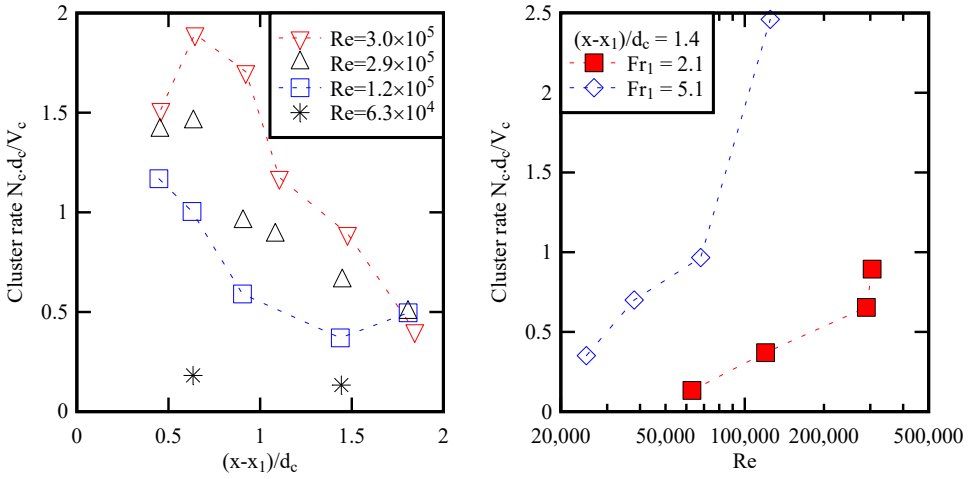

(A, Left) Dimensionless bubble cluster flux (i.e. number of cluster per second) $N_c \times d_1/V_1$ as a function of the dimensionless distance from the jump toe $(x\text{-}x_1)/d_c$

(B, Right) Dimensionless bubble cluster flux (i.e. number of cluster per second) $N_c \times d_1/V_1$ as a function of the Reynolds number at $(x\text{-}x_1)/d_c = 1.4$ - Comparison with the data of Chanson and Chachereau (2013) for $Fr_1 = 5.1$

Fig. 14. Bubble clustering properties in the air-water shear layer of hydraulic jump $Fr_1 = 2.1$ at the location $y = Y_{Fmax}$ where $F = F_{max}$.

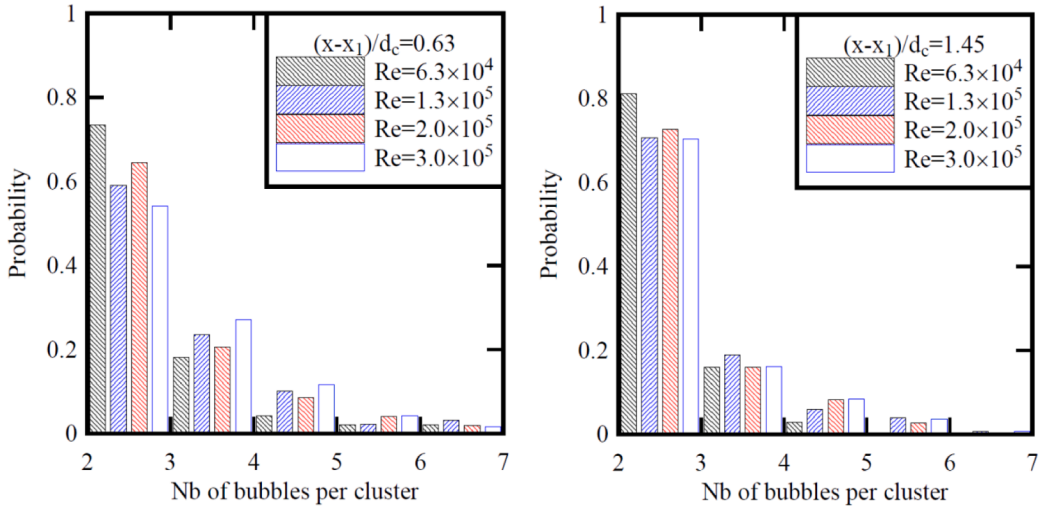

(A, Left) $(x\text{-}x_1)/d_c = 0.63$

(B, Right) $(x\text{-}x_1)/d_c = 1.45$

Fig. 15. Histogram of number of bubbles per cluster in the air-water shear layer of hydraulic jump $Fr_1 = 2.1$ at the location $y = Y_{Fmax}$ where $F = F_{max}$.

with the Reynolds number at a given dimensionless location $(x\text{-}x_1)/d_c$ for a given Froude number $Fr_1 = 2.1$, without asymptotic trend. The present findings are summarised in Table 2 and discussed in the following paragraphs. In Table 5-1, the absence of similarity, implying the presence of major scale effects, are highlighted in Red.

For $7.75 \times 10^3 < Re < 3.05 \times 10^5$, the flow patterns and free-surface measurements showed both similarity and scale effects, depending upon the relevant dependant dimensionless parameter. The ratio of downstream to upstream depths d_2/d_1 was not affected by the Reynolds number. The experimental observations showed some longitudinal profile of the roller surface which were very similar for all Reynolds numbers. But the dimensionless lengths of the roller and of the bubbly flow region increased with increasing Reynolds numbers.

For $6.3 \times 10^4 < Re < 3.05 \times 10^5$, the comparative air-water flow measurements provided some clear trend. The void fraction data presented the same distribution shapes for $Re > 6.3 \times 10^4$ (i.e. Eqs. (8), (13) & (14)). While the shape of the void fraction distribution was similar for $Re > 6.3 \times 10^4$ herein, some characteristic void fraction feature presented differences. The maximum void fraction in the air-water shear layer C_{max} was underestimated at the smallest scale, i.e. $Re = 6.3 \times 10^4$, and similarity was achieved for $Re > 1.2 \times 10^4$ (Fig. 7).

The bubble count rate distribution presented some similar profiles for

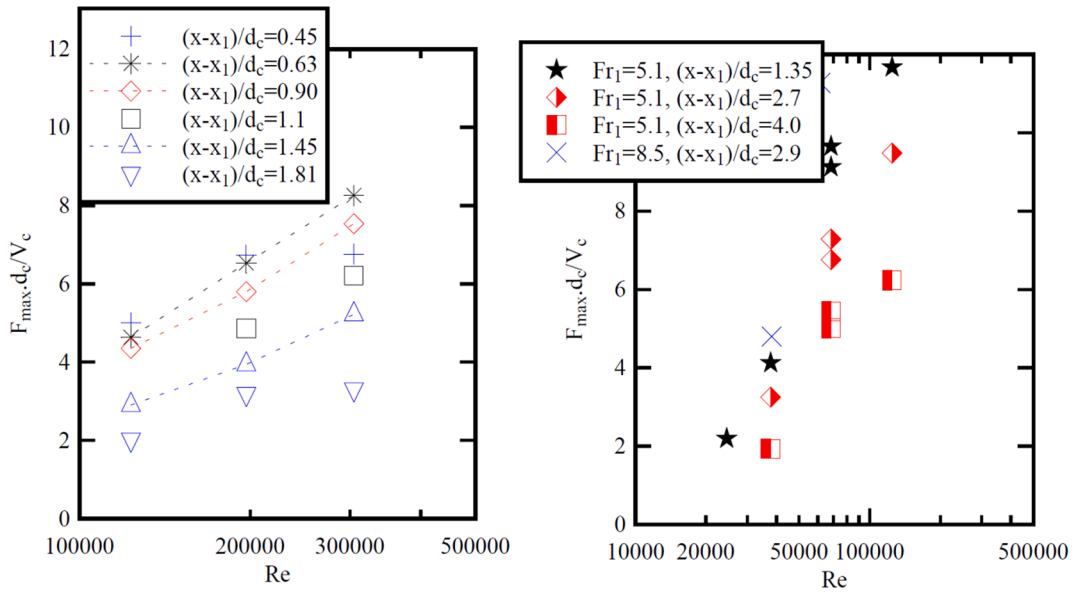

Fig. 16. Effects of the Reynolds number on the maximum void bubble count rate $F_{max} \times d_c/V_c$ in the air-water shear layer. (A, Left) $Fr_1 = 2.1$ (Present study); (B, Right) Past studies [25,46,24].

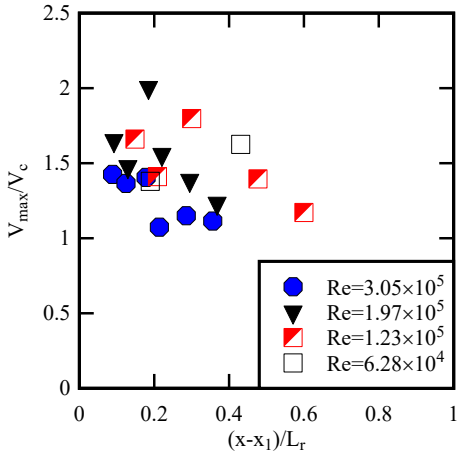

Fig. 17. Longitudinal decay in maximum interfacial velocity in the air-water shear layer as a function of the relative position along the roller $(x\text{-}x_1)/L_r$ in a hydraulic jump with $Fr_1 = 2.1$.

$Re > 6.3 \times 10^4$, the same similarity being previously reported with $Fr = 5.1$ to 8.5 for $Re > 2.5 \times 10^4$ [25]. However, the dimensionless maximum bubble count rate data $F_{max} \times d_c/V_c$ showed an increasing trend with increasing Reynolds number at a given dimensionless location $(x\text{-}x_1)/d_c$ without any upper limit (Fig. 16A). The finding was on par with previous observations in hydraulic jumps at higher Froude numbers [25,46,24] (Fig. 16B). (Interestingly, all these studies were performed with similar phase-detection conductivity probe systems, equipped with comparable probe tip sizes, i.e. between 0.25 mm and 0.35 mm, and sampled at a minimum sampling rate of 20 kHz per sensor.) The data indicated an increase in maximum bubble count rate as a power law function of the Reynolds number. For $2.1 < Fr_1 < 5.1$ and $(x\text{-}x_1)/d_c = 1.4$, and the data shown in Fig. 16, the trend was best correlated by:

$$\frac{F_{max} \times d_c}{V_c} = 0.00145 \times Re^{(0.555+0.0434 \times Fr_1)} \quad \text{for } 2.1 < Fr_1 < 5.1 \text{ at } (x - x_1)/d_c = 1.4 \tag{17}$$

with a normalised correlation coefficient $R = 0.952$.

The vertical distributions of interfacial velocity presented a profile following that of a wall jet, close to earlier findings [53,22]. The maximum velocity in the air-water shear region V_{max}/V_c decreased quasi-exponentially with increasing longitudinal distance along the roller [66,74] (Fig. 17). No obvious scale effect was noted (Fig. 11).

The turbulence intensity Tu distributions presented some qualitative similarity for all experiments, with increasing turbulence intensity with increasing distance from the bed. However, the turbulence levels were systematically underestimated at the lowest Reynolds numbers, and the vertical profiles did not reach asymptotic values at the highest Reynolds numbers. The turbulent time scale data $T_{xx} \times V_c/d_c$ showed some overestimation at the lowest Reynolds numbers, as illustrated in Fig. 18. Some similarity was observed both qualitatively and quantitatively for $Re > 2 \times 10^5$.

The distributions of bubble chord lengths exhibited close quantitative dimensional data for all Reynolds numbers (Fig. 13). Although of millimetric sizes, the bubbles were comparatively smaller at the largest Reynolds numbers. That is, the bubble chord times and chord lengths did not scale as $(X_R)^{1/2}$ and X_R respectively, as a Froude similarity would require, with X_R the geometric length scale ratio. The effects of the Reynolds number on the bubble clustering characteristics were systematically checked. Typical results are presented in Fig. 19, in the form of the dimensionless number of cluster per second $N_c \times d_c/V_c$, average number of bubbles per cluster and percentage of bubbles in clusters. All three dimensionless bubble cluster properties in the air-water shear layer presented major scale effects, according to a Froude similitude. Basically, the dimensionless number of clusters per second, number of bubbles per cluster, and percentage of bubbles in cluster tended to increase monotonically with the Reynolds number at a given dimensionless location $(x\text{-}x_1)/d_c$ for a given Froude number (Fig. 19). Such a result was previously reported at higher Froude numbers [24,66]. Bubble clustering affected a comparatively larger proportion of particles at high Reynolds numbers, suggesting that the interactions between entrained bubbles and turbulent structures were not scaled accurately based upon a Froude similitude.

Altogether, the present results (Table 2) have some major implication on engineering designs, because many water engineering structures, including culverts, storm waterways, weirs, and water treatment plants, operate with Reynolds numbers in excess of 10^5, with larger structures operating with Re over 10^8. While seminal, the hydraulic jump remains today a hydrodynamic challenge to researchers and engineers. The correct design of hydraulic jump stilling structures is a

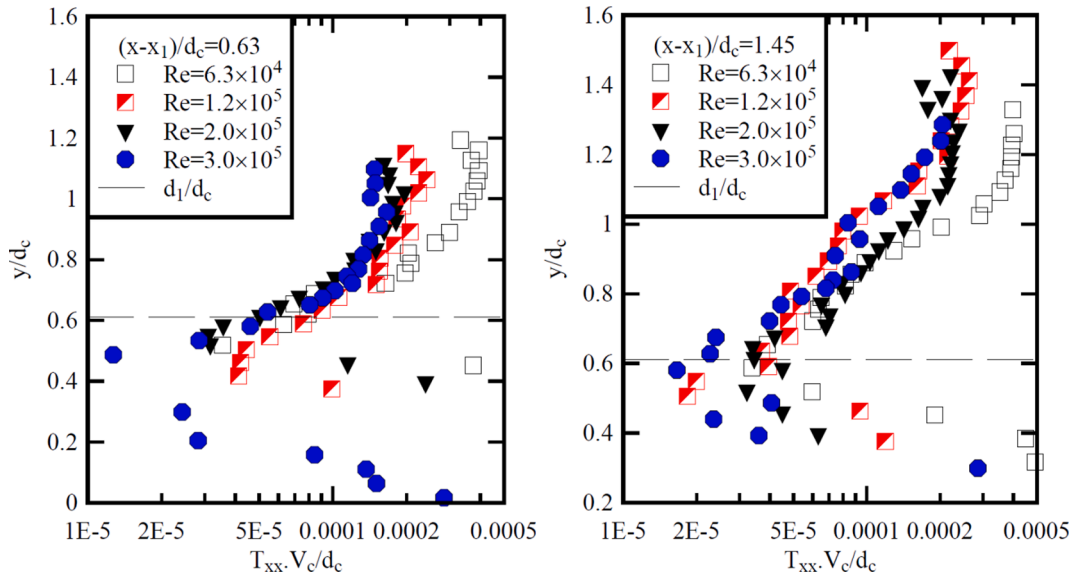

Fig. 18. Dimensionless distributions of turbulent time scale $T_{xx} \times V_c/d_c$ for $Fr_1 = 2.1$ at $(x\text{-}x_1)/d_c = 0.63$ (Left) and 1.45 (Right). Comparison between experiments at different Reynolds numbers.

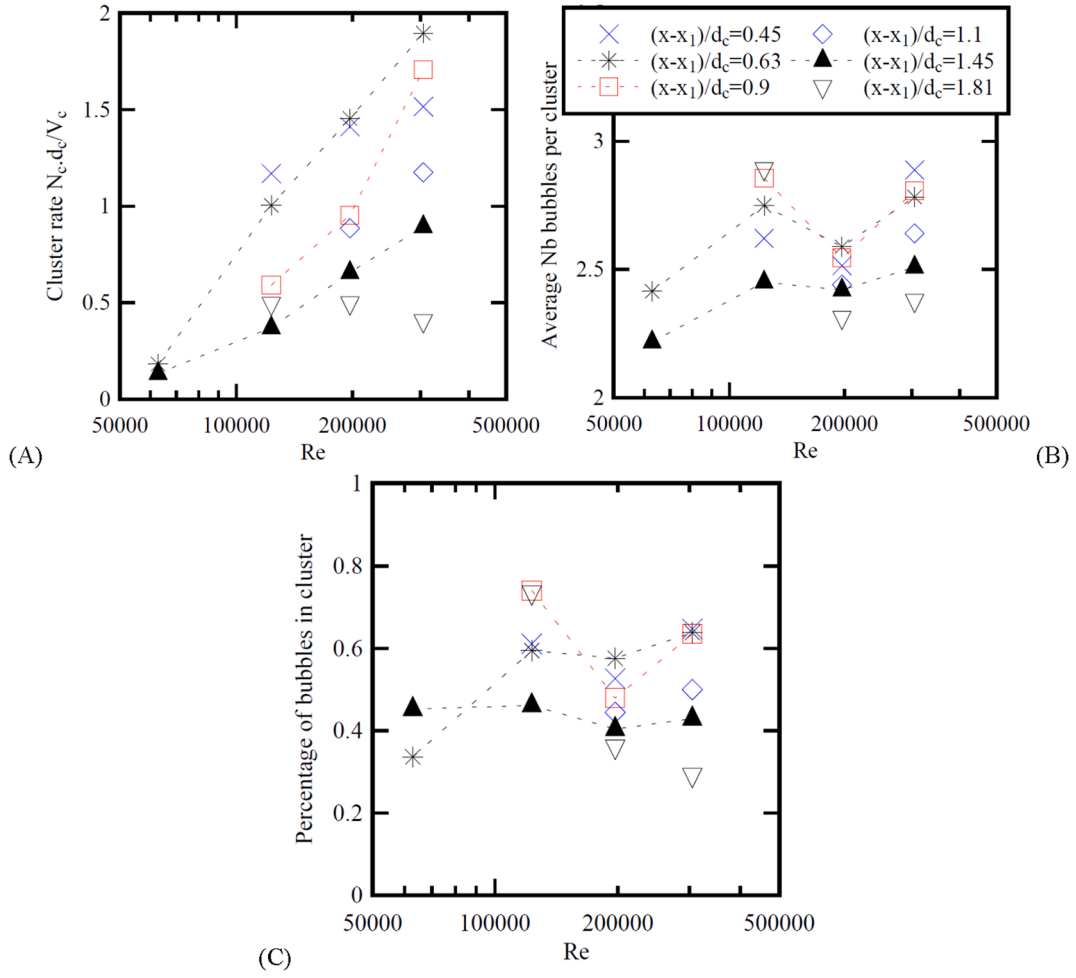

Fig. 19. Effects of the Reynolds number on bubble clustering properties in the air-water shear layer of hydraulic jump at the location $y = Y_{Fmax}$ where $F = F_{max}$ for Fr = 2.1. Same legend for all graphs. (A) Dimensionless number of cluster per second $N_c \times d_c/V_c$; (B) Average number of bubbles per cluster; (C) Percentage of bubbles in clusters.

Table 2
. Physical scaling of hydraulic jumps based on a Froude similarity - Studies in smooth horizontal rectangular channels.

Air-water flow properties	Notation	Fr_1	Re	Criterion to minimise scale effects ([1])	Recommendation / Equation	Reference
• Ratio of conjugate depth	d_2/d_1	2.1 to 8.5	7.75×10^3 to 3.0×10^5	No scale effect	Bélanger equation	[Present], [WC16], [CG08]
• Roller length	L_r/d_c	2 to 5.1	7.75×10^3 to 3.0×10^5	N/A	Full scale testing X_R=1	[Present], [MU07], [WC15]
• Bubbly flow length	L_a/d_c	2.1	7.75×10^3 to 3.0×10^5	N/A	Full scale testing X_R=1	[Present], [C09]
• Fluctuation frequency of longitudinal jump toe position	$F_{toe}\times d_c/V_c$	2.1	7.75×10^3 to 3.0×10^5	N/A	Full scale testing X_R=1	[Present]
• Roller surface profile	d/d_c	2.1	7.75×10^3 to 3.0×10^5	No scale effect	Power law Eq. (5-2)	[Present]
• Void fraction distribution	$C=f_1(y/d_c)$	2.1 5.1 to 8.5	6.3×10^4 to 3.0×10^5 2.5×10^4 to 1×10^5	$Re > 6.3\times10^4$ $Re > 2.7\times10^4$	Advective diffusion Eqs. (4-1), (4-5) & (4-6)	[Present] [CG08]
• Maximum void fraction in shear layer	C_{max}	2.1	6.3×10^4 to 3.0×10^5	$Re > 1.2\times10^5$	Eq. (4-9)	[Present]
• Depth-averaged void fraction	C_{mean}	2.1	6.3×10^4 to 3.0×10^5	$Re > 1.2\times10^5$		[Present]
• Bubble count rate distribution	$F\times d_c/V_c=f_2(y/d_c)$	2.1 5.1 to 8.5	6.3×10^4 to 3.0×10^5 2.5×10^4 to 1×10^5	$Re > 6.3\times10^4$ $Re > 2.7\times10^4$		[Present] [CG08]
• Maximum bubble count rate in shear layer	$F_{max}\times d_c/V_c$	2.1 to 8.5	2.5×10^4 to 3.0×10^5	N/A	Full scale testing X_R=1	[Present], [CG08], [MC08], [CC13]
• Interfacial velocity distribution	$V/V_c=f_3(y/d_c)$	2.1 to 8.5	3.4×10^4 to 3.0×10^5	No scale effect	Wall jet	[Present], [MC08], [CC13], [WC16]
• Maximum velocity in shear layer	V_{max}/V_c	2.1 to 8.5	3.4×10^4 to 3.0×10^5	No scale effect	Exponential decay	[Present], [WC16]
• Turbulent intensity distribution	$Tu=f_4(y/d_c)$	2.1	6.3×10^4 to 3.0×10^5	N/A	Full scale testing X_R=1	[Present]
• Turbulent time scale distribution	$T_{xx}\times V_c/d_c=f_5(y/d_c)$	2.1	3.4×10^4 to 3.0×10^5	$Re > 2\times10^5$		[Present]
• Bubble chord times	$t_{ch\text{-}a}\times V_c/d_c$	2.1 to 8.5	3.4×10^4 to 3.0×10^5	N/A	Full scale testing X_R=1	[Present], [MC08], [CC13], [WC16]
• Bubble chord lengths		2.1 to 8.5	3.4×10^4 to 3.0×10^5	N/A	Full scale testing X_R=1	[Present], [MC08], [CC13], [WC16]
• Clustering rate	$N\times d_c/V_c$	2.1	7.75×10^3 to 3.0×10^5	N/A	Full scale testing X_R=1	[Present], [CC13], [WC16]
• Average number of bubbles per cluster		2.1	7.75×10^3 to 3.0×10^5	N/A	Full scale testing X_R=1	[Present], [CC13], [WC16]
• Percentage of clustered bubbles		2.1	7.75×10^3 to 3.0×10^5	N/A	Full scale testing X_R=1	[Present], [CC13], [WC16]

Notes: ([1]): for application to full-scale prototype hydraulic structures.
References: [Present] Present study, [CG08] Chanson and Gualtieri [25]; [MU07] Murzyn et al. [48]; [MC09] Murzyn and Chanson [46]; [C09] Chanson [17]; [CC13] Chanson and Chachereau [24]; [WC15] Wang and Chanson [64]; [WC16] Wang and Chanson [66].

matter of critical importance, that relies upon sound modelling. The present results extended earlier limited studies and demonstrated that the kinematic and dynamic similarity of air-water flows in hydraulic jumps cannot be obtained with a Froude similarity. Instead, there is an urgent need for new field observations performed in situ in prototype structures, because "*no prototype data means no definite validation of any kind of modelling!*" ([20], p.237). In other words, full-scale air-water flow measurements are required in hydraulics jumps operating at Reynolds numbers well over 10^6, to complement current studies, including the present one (Table 1).

6. Conclusion

A hydraulic jump is a complicated turbulent physical process. The breaking region, called the roller, includes typically a developing air-water shear layer and a recirculation region above. The present physical study is based upon a new experimental data set performed with the double objective of: (1) characteristing experimentally the air-water flow characteristics in hydraulic jumps with a small Froude number ($Fr_1 = 2.1$) and (2) discussing the potential scale effects involving several Reynolds numbers ($7.8 \times 10^3 < Re < 3.05 \times 10^5$) for $Fr_1 = 2.1$. Four unique and novel traits of the current investigation were the low Froude number $Fr_1 = 2.1$, the very wide range of Reynolds numbers tested systematically, the broad amount of air-water flow properties investigated, and the relatively high Reynolds number ($Re = 3.05 \times 10^5$) achieved in the largest experiment.

In the roller region, some distinct air-water flow patterns were observed with $Fr_1 = 2.1$, generally similar to those observed in hydraulic jumps at higher Froude numbers. At the upstream end of the roller, i.e. $(x\text{-}x_1)/L_r < 0.2$, the void fraction data showed some vertical profiles from a convex shape. Further downstream of the roller toe, i.e. $0.2 < (x\text{-}x_1)/L_r$, two distinct air-water regions were observed in the roller region: one on the upper part of the roller and another in the developing shear region. The air entrainment within the roller was a combination air entrapment and convective diffusion of bubbles in the air-water shear layer, and interfacial aeration through the upper free-surface. In the downstream end of the roller, i.e. $0.4 < (x\text{-}x_1)/L_r$, the air bubble motion was mostly driven by buoyancy and interfacial de-aeration. The bubble count rate, size and clustering data showed a highly fragmented two-phase gas–liquid flow in the roller. The intensity of bubble clustering delivered a measure of bubble-turbulence inter-relations and the present data highlighted a large proportion of clustered particles, especially at higher Reynolds numbers.

Overall, this current study presents the most extensive study of similarity and scale effects in a hydraulic jump. Similarity and scale effects were tested in terms of a broad range of hydraulic and air-water flow properties in the hydraulic jump with constant Froude and Morton numbers, i.e. $Fr_1 = 2.1$ & $Mo = 2.5 \times 10^{-11}$, but different Reynolds numbers, i.e. $0.078 \times 10^5 < Re < 3.05 \times 10^5$ (Table 1). More than two dozen of parameters were tested systematically under Froude similar

conditions (Table 2). All the data demonstrated that the selection of relevant air-water flow property(ies) used to assess similarity and scale effects is most essential [20,17]. Further the concept of similarity and scale effects must be linked to specific flow conditions. In a hydraulic jump at low Froude number $Fr_1 = 2.1$ in a smooth channel, the present results (Table 2) showed that many hydraulic jump properties could not be extrapolated from laboratory study to full scale hydraulic structures without substantial scale effects. The findings have profound implications for engineering design applications, often operating with Reynolds numbers in excess of 10^5, and associated with intense dissipation processes, e.g. hydraulic jump stilling basins. Basically, there is an urgent need for "*field measurements of high quality*" because "*there remain some critical issues with the validity of extrapolation of physical model results to prototype flow conditions, as well as with the validity of numerical results calibrated with and tested against small-scale laboratory data*" ([20], p. 223 & p. 237).

CRediT authorship contribution statement

Jorge Estrella: Validation, Formal analysis, Investigation, Data curation, Writing – original draft, Writing - review & editing, Visualization. **Davide Wüthrich:** Conceptualization, Methodology, Formal analysis, Writing – original draft, Writing - review & editing, Supervision, Funding acquisition. **Hubert Chanson:** Conceptualization, Methodology, Formal analysis, Resources, Data curation, Writing – original draft, Writing - review & editing, Supervision, Visualization, Funding acquisition.

Declaration of Competing Interest

The authors declare that they have no known competing financial interests or personal relationships that could have appeared to influence the work reported in this paper.

Acknowledgements

The authors would like to thank Professor Michael Pfister (University of Applied Sciences and Arts Western Switzerland, Fribourg), and Professor Carlo Gualtieri (University of Napoli Federico II, Italy), for their helpful comments and suggestions. They thank Mr Rui (Ray) Shi (The University of Queensland) for technical discussion and input. The authors acknowledge the technical assistance of Jason Van Der Gevel and Stewart Matthews (The University of Queensland). The financial support of the Swiss National Science Foundation (Grant P2ELP2_181794) and of the University of Queensland, School of Civil Engineering is acknowledged.

References

[1] B.A. Bakhmeteff, Hydraulics of Open Channels, McGraw-Hill, New York, USA, 1st ed., 1932, 329 pages.
[2] B.A. Bakhmeteff, A.E. Matzke, The hydraulic jump in terms of dynamic similarity, Transactions, ASCE, Vol. 101, pp. 630-647. Discussion: Vol. 101, 1936, pp. 648-680.
[3] J. Bertrand, Sur l'homogénéité dans les formules de physique. Comptes rendus, 86 (15) (1878) 916–920.
[4] T. Brattberg, H. Chanson, L. Toombes, Experimental investigations of free-surface aeration in the developing flow of two-dimensional water jets, J. Fluids Eng., Trans. ASME, 120(4) (1998) pp. 738-744, doi:10.1115/1.2820731.
[5] M. Brocchini, Free surface boundary conditions at a bubbly/weakly splashing air-water interface, Phys. Fluids, 14(6) (2002) 1834-1840.
[6] M. Brocchini, D.H. Peregrine, The dynamics of strong turbulence at free surfaces. Part 1. Description, J. Fluid Mech., 449 (2001) 225-254.
[7] P. Cain, I.R. Wood, Measurements of self-aerated flow on a spillway, Jl. Hyd. Div., ASCE, 107, HY11 (1981) 1425-1444.
[8] E. Calzavarini, T.H. van der Berg, F. Toschi, D. Lohse, Quantifying microbubble clustering in turbulent flow from single-point measurements, Phys. Fluids, 20(4) (2008), Paper 040702, 6 pages. Doi: 10.1063/1.2911036.
[9] Y. Chachereau, H. Chanson, Bubbly flow measurements in hydraulic jumps with small inflow froude numbers. Int. J. Multiphase Flow, 37(6) (2011) 555-564 Doi: 10.1016/j.ijmultiphaseflow.2011.03.012.
[10] H. Chanson, Self-aerated flows on chutes and spillways, J. Hydraulic Eng., ASCE, 119(2) (1993) 220-243, Doi: 10.1061/(ASCE)0733-9429(1993)119:2(220).
[11] H. Chanson, Air bubble entrainment in free-surface turbulent shear flows, Academic Press, London, UK, 1997, 401 pages.
[12] H. Chanson, Physical modelling of hydraulics. in "The Hydraulics of Open Channel Flow: An Introduction." Edward Arnold, London, UK, 1999, pp. 261-283.
[13] H. Chanson, Air-water flow measurements with intrusive phase-detection probes. Can we Improve their Interpretation? J. Hydraulic Eng., ASCE, 128(3) (2002) 252-255, Doi: 10.1061/(ASCE)0733-9429(2002)128:3(252).
[14] H. Chanson, Unsteady air-water flow measurements in sudden open channel flows, Exp. Fluids, 37(6) (2004) 899-909.
[15] H. Chanson, Air-water and momentum exchanges in unsteady surging waters: an experimental study, Exp. Therm. Fluid Sci., 30(1) (2005) 37-47.
[16] H. Chanson, Bubbly flow structure in hydraulic jump, Eur. J. Mech. B/Fluids, 26(3) (2007) 367–384, doi:10.1016/j.euromechflu.2006.08.001.
[17] H. Chanson, Turbulent air-water flows in hydraulic structures: dynamic similarity and scale effects, Environ. Fluid Mech. 9(2) (2009) 125-142, doi: 10.1007/s10652-008-9078-3.
[18] H. Chanson, Convective transport of air bubbles in strong hydraulic jumps, Int. J. Multiphase Flow, 36(10) (2010) 798-814, Doi: 10.1016/j.ijmultiphaseflow.2010.05.006.
[19] H. Chanson, Momentum considerations in hydraulic jumps and bores, J. Irrigation and Drainage Eng., ASCE 138 (4) (2012) 382–385, https://doi.org/10.1061/(ASCE)IR.1943-4774.0000409.
[20] H. Chanson, Hydraulics of aerated flows: qui pro quo? J. Hydraulic Res., IAHR, Invited Vision paper 51 (3) (2013) 223–243, https://doi.org/10.1080/00221686.2013.795917.
[21] H. Chanson, S. Aoki, A. Hoque, Bubble entrainment and dispersion in plunging jet flows: freshwater versus seawater, J. Coastal Res. 22 (3) (2006) 664–677, https://doi.org/10.2112/03-0112.1.
[22] H. Chanson, T. Brattberg, Experimental study of the air-water shear flow in a hydraulic jump, Int. J. Multiphase Flow 26 (4) (2000) 583–607, https://doi.org/10.1016/S0301-9322(99)00016-6.
[23] H. Chanson, G. Carosi, Advanced post-processing and correlation analyses in high-velocity air-water flows, Environ. Fluid Mech. 7 (6) (2007) 495–508, https://doi.org/10.1007/s10652-007-9038-3.
[24] H. Chanson, Y. Chachereau, Scale effects affecting two-phase flow properties in hydraulic jump with small inflow froude number, Exp. Therm. Fluid Sci. 45 (2013) 234–242, https://doi.org/10.1016/j.expthermflusci.2012.11.014.
[25] H. Chanson, C. Gualtieri, Similitude and scale effects of air entrainment in hydraulic jumps, J. Hydraulic Res., IAHR 46 (1) (2008) 35–44.
[26] H. Chanson, L. Toombes, Air-water flows down stepped chutes: turbulence and flow structure observations, Int. J. Multiphase Flow 28 (11) (2002) 1737–1761, https://doi.org/10.1016/S0301-9322(02)00089-7.
[27] H. Chanson, L. Toombes, Strong interactions between free-surface aeration and turbulence in an open channel flow, Exp. Therm. Fluid Sci. 27 (5) (2003) 525–535, https://doi.org/10.1016/S0894-1777(02)00266-2.
[28] C. Crowe, M. Sommerfield, Y. Tsuji, Multiphase Flows with Droplets and Particles, CRC Press, Boca Raton, USA, 1998, p. 471.
[29] P.D. Cummings, H. Chanson, Air entrainment in the developing flow region of plunging jets. Part 1: theoretical development, J. Fluids Eng., Trans. ASME 119 (3) (1997) 597–602, https://doi.org/10.1115/1.2819286.
[30] D.A. Ervine, A.A. Ahmed, A scaling relationship for a two-dimensional vertical dropshaft, Proc. Intl. Conf. on Hydraulic Modelling of Civil Engineering Structures, BHRA Fluid Eng., Coventry, UK, paper E1, 1982, pp. 195-214.
[31] J. Estrella, D. Wüthrich, H. Chanson, Two-phase air-water flow properties in hydraulic jump at low froude number: scale effects in physical modelling, Hydraulic Model Report No. CH120/21, School of Civil Engineering, The University of Queensland, Brisbane, Australia, 157 pages & 4 video movies, 2021, DOI: 10.14264/b6bf13f, (ISBN 978-1-74272-345-7).
[32] S. Felder, H. Chanson, Air–water flow characteristics in high-velocity free-surface flows with 50% void fraction, Int. J. Multiph. Flow 85 (2016) 186–195, https://doi.org/10.1016/j.ijmultiphaseflow.2016.06.004.
[33] John Foss, Ronald Panton, Alexander Yarin, Nondimensional representation of the boundary-value problem, in: Cameron Tropea, Alexander L. Yarin, John F. Foss (Eds.), Springer Handbook of Experimental Fluid Mechanics, Springer Berlin Heidelberg, Berlin, Heidelberg, 2007, pp. 33–82, https://doi.org/10.1007/978-3-540-30299-5_2.
[34] C. Gualtieri, H. Chanson, Effect of froude number on bubble clustering in a hydraulic jump, J. Hydraulic Res., IAHR 48 (4) (2010) 504–508, https://doi.org/10.1080/00221686.2010.491688.
[35] F.M. Henderson, Open Channel Flow, MacMillan Company, New York, USA, 1966.
[36] J.W. Hoyt, R.H.J. Sellin, Hydraulic jump as 'mixing layer', J. Hydraulic Eng., ASCE 115 (12) (1989) 1607–1614.
[37] A.A. Kalinske, J.M. Robertson, Closed conduit flow, Trans., ASCE 108 (1943) 1435–1447.
[38] H. Kipphan, F. Mesch, Flow Measurements using Transit Time Correlation, in: H.H. Dijstelbergen, E.A. Spencer (Eds.), Flow Measurements of Fluids, North Holand Publ. Co., 1978, pp. 409-416.
[39] X. Leng, H. Chanson, Air-Water Interaction and Characteristics in Breaking Bores, International Journal of Multiphase Flow 120 (2019) 17, https://doi.org/10.1016/j.ijmultiphaseflow.2019.103101. Paper 103101.
[40] J.A. Liggett, Fluid mechanics, McGraw-Hill, New York, USA, 1994.
[41] J. Lighthill, Waves in Fluids, Cambridge University Press, 1978, p. 504.

[42] P. Lubin, O. Kimmoun, F. Veron, S. Glockner, Discussion on Instabilities in Breaking Waves: Vortices, Air-entrainment and Droplet Generation, Eur. J. Mech. / B Fluids 73 (2019) 144–156, https://doi.org/10.1016/j.euromechflu.2018.05.006.
[43] L. Montano, S. Felder, An experimental study of air-water flows in hydraulic jumps on flat slopes, J. Hydraulic Res., IAHR 58 (5) (2020) 767–777, https://doi.org/10.1080/00221686.2019.1671512.
[44] M. Mortazavi, V. Le Chenadec, P. Moin, A. Mani, Direct numerical simulation of a turbulent hydraulic jump: turbulence statistics and air entrainment, J. Fluid Mech. 797 (2016) 60–94, https://doi.org/10.1017/jfm.2016.230.
[45] M. Mossa, U. Tolve, Flow visualization in bubbly two-phase hydraulic jump, J. Fluids Eng., ASME 120 (1998) 160–165.
[46] F. Murzyn, H. Chanson, Experimental assessment of scale effects affecting two-phase flow properties in hydraulic jumps, Exp. Fluids 45 (3) (2008) 513–521, https://doi.org/10.1007/s00348-008-0494-4.
[47] F. Murzyn, D. Mouaze, J.R. Chaplin, Optical Fibre probe measurements of bubbly flow in hydraulic jumps, Int. J. Multiph. Flow 31 (1) (2005) 141–154.
[48] F. Murzyn, D. Mouazé, J.R. Chaplin, Air-water interface dynamic and free surface features in hydraulic jumps, J. Hydraul. Res., IAHR 45 (5) (2007) 679–685.
[49] P. Novak, J. Cabelka, Models in Hydraulic Engineering. Physical Principles and Design Applications, Pitman Publ, London, UK, 1981, p. 459.
[50] I. Ohtsu, Y. Yasuda, S. Awazu, Free and submerged hydraulic jumps in rectangular channels, Report of Research Inst. of Science and Technology, No. 35, Nihon University, Japan, Feb., 1990, 50 pages.
[51] M. Pfister, H. Chanson, Two-phase air-water flows: scale effects in physical modeling, J. Hydrodynamics 26 (2) (2014) 291–298, https://doi.org/10.1016/S1001-6058(14)60032-9.
[52] N. Rajaratnam, An experimental study of air entrainment characteristics of the hydraulic jump, J. Inst. Engineers India 42 (7) (1962) 247–273.
[53] N. Rajaratnam, The hydraulic jump as a wall jet, J. Hydraulic Division, ASCE, Vol. 91, No. HY5, pp. 107-132. Discussion: Vol. 92, No. HY3, pp. 110-123 & Vol. 93, No. HY1, 1965, pp. 74-76.
[54] N.S.L. Rao, H.E. Kobus, "Characteristics of Self-Aerated Free-Surface Flows." Water and Waste Water/Current Research and Practice, Vol. 10, Eric Schmidt Verlag, Berlin, Germany, 1974, pp. 224.
[55] Rayleigh, Lord, The principle of similitude, Nature, No. 2368, Vol. 95, 1912, pp. 66-68.
[56] F.J. Resch, H.J. Leutheusser, "Le Ressaut Hydraulique : mesure de Turbulence dans la Région Diphasique." ('The Hydraulic Jump : Turbulence Measurements in the Two-Phase Flow Region'.), Jl La Houille Blanche 4 (1972) 279–293 (in French).
[57] H. Rouse, Fluid Mechanics for Hydraulic Engineers, McGraw-Hill Publ., New York, USA (also Dover Publ., New York, USA, 1961, 422 pages), 1938.
[58] H. Rouse, T.T. Siao, S. Nagaratnam, Turbulence characteristics of the hydraulic jump, Trans., ASCE 124 (1959) 926–950.
[59] R. Schröder, Die turbulente Strömung im freien Wechselsprung, Mitteilungen, No. 59, Institut für Wasserbau und Wasserwirtschaft, Tech. Univ. Berlin, Germany (in German), 1963.
[60] R. Shi, D. Wüthrich, H. Chanson, "Air-water characteristics of a breaking bore roller. Part II: Air-water flow properties." *Hydraulic Model Report No. CH118/20*, School of Civil Engineering, The University of Queensland, Brisbane, Australia, 2021, p. 160 pages..
[61] S. Sun, H. Chanson, Characteristics of Clustered Particles in Skimming Flows on a Stepped Spillway, Environ. Fluid Mech. 13 (1) (2013) 73–87, https://doi.org/10.1007/s10652-012-9255-2.
[62] L. Toombes, Experimental study of air-water flow properties on low-gradient stepped cascades, Ph.D. thesis, Dept of Civil Engineering, The University of Queensland, Brisbane, Australia, 2002.
[63] B.L. Valle, G.B. Pasternack, Air concentrations of submerged and unsubmerged hydraulic jumps in a bedrock step-pool channel, J. Geophys. Res., Vol. 111, No. F3, paper F030l6, 2006, 12 pages (DOI: 10.1029/2004JF000140).
[64] H. Wang, H. Chanson, Air entrainment and turbulent fluctuations in hydraulic jumps, Urban Water J. 12 (6) (2015) 502–518, https://doi.org/10.1080/1573062X.2013.847464.
[65] H. Wang, H. Chanson, Experimental study of turbulent fluctuations in hydraulic jumps, J. Hydraulic Eng., ASCE, Vol. 141, No. 7, Paper 04015010, 2015b, 10 pages (DOI: 10.1061/(ASCE)HY.1943-7900.0001010).
[66] H. Wang, H. Chanson, Self-similarity and scale effects in physical modelling of hydraulic jump roller dynamics, air entrainment and turbulent scales, Environ. Fluid Mech. 16 (6) (2016) 1087–1110, https://doi.org/10.1007/s10652-016-9466-z.
[67] H. Wang, H. Chanson, Characterisation of transverse turbulent motion in quasi-two-dimensional aerated flow: application of four-point air-water flow measurements in hydraulic jump, Exp. Therm. Fluid Sci. 100 (2019) 222–232, https://doi.org/10.1016/j.expthermflusci.2018.09.004.
[68] H. Wang, Z. Hu, H. Chanson, Two-dimensional bubble clustering in hydraulic jumps, Exp. Therm Fluid Sci. 68 (2015) 711–721, https://doi.org/10.1016/j.expthermflusci.2015.07.006.
[69] I.R. Wood, Air Water Flows, Proc. 21st IAHR Congress, Melbourne, Australia, Keynote address, 1985, pp. 18-29.
[70] I.R. Wood, Air entrainment in free-surface flows, IAHR Hydraulic Structures Design Manual No. 4, Hydraulic Design Considerations, Balkema Publ., Rotterdam, The Netherlands, 1991, 149 pages.
[71] S. Wu, N. Rajaratnam, Transition from hydraulic jump to open channel flow, J. Hydraulic Eng., ASCE, 122(9) (1996) 526-528.
[72] D. Wüthrich, R. Shi, H. Wang, CHANSON, Three-dimensional air-water flow properties of a hydraulic jump with low Froude numbers and relatively high Reynolds numbers, Proceedings of the 8th IAHR International Symposium on Hydraulic Structures ISHS2020, 12-15 May 2020, Santiago, Chile, R. JANSSEN and H. CHANSON Editors, The University of Queensland, Brisbane, Australia, 10 pages, 2020a, Doi: 10.14264/uql.2020.583.
[73] D. Wüthrich, R. Shi, H. Chanson, "Air-water characteristics of a breaking bore roller. Part I: Two-phase surface features and strong turbulence." Hydraulic Model Report No. CH117/20, School of Civil Engineering, The University of Queensland, Brisbane, Australia, 2020, p. 134 pages.
[74] G. Zhang, H. Wang, H. Chanson, Turbulence and Aeration in Hydraulic Jumps: Free-Surface Fluctuation and Integral Turbulent Scale Measurements, Environmental Fluid Mechanics, 13(2) (2013) 189–204, doi: 10.1007/s10652-012-9254-3.
[75] H. Wang, Turbulence and Air Entrainment in Hydraulic Jumps, Ph.D. thesis, School of Civil Engineering, The University of Queensland, Brisbane, Australia, 341 pages & Digital appendices, 2014, doi: 10.14264/uql.2014.542.